UNIVERSITY OF GENOVA

PHD PROGRAM IN BIOENGINEERING AND ROBOTICS

Leveraging Additive Manufacturing in Industry to Create Enhanced-Performance Components

by

Emilio Ottonello

Thesis submitted for the degree of *Doctor of Philosophy* (37° cycle)

February 2026

Alberto Parmiggiani	Supervisor
Paolo Massobrio	Head of the PhD program

Thesis Jury:

Carlo Canali, *Italian Institute of Technology*	External examiner
Jovana Jovanova, *Delft University of Technology*	External examiner
Enrico Lertora, *University of Genoa*	Internal examiner

Dibris

Department of Informatics, Bioengineering, Robotics and Systems Engineering

I would like to dedicate this thesis to my wife, Giulia, who is the most beautiful person I have ever met. I owe her my entire life. I love you, Cu.

Declaration

I hereby declare that except where specific reference is made to the work of others, the contents of this dissertation are original and have not been submitted in whole or in part for consideration for any other degree or qualification in this, or any other university. This dissertation is my own work and contains nothing which is the outcome of work done in collaboration with others, except as specified in the text and Acknowledgements. This dissertation contains fewer than 65,000 words including appendices, bibliography, footnotes, tables and equations and has fewer than 150 figures.

Emilio Ottonello
February 2026

Abstract

AM technology enables the production of complex structures layer-by-layer, thus transforming traditional manufacturing methods and offering unprecedented design freedom and material efficiency. This research aims to bridge the gap between AM's theoretical capabilities and practical applications in the robotic and industrial fields, where AM can reduce mechanical complexity, optimise performance, and increase part reliability. In particular, the potential of additive manufacturing (AM) in robotics is explored, focusing on two key innovations: monolithic mechanisms with compliant joints and non-planar additive manufacturing.

Monolithic mechanisms, manufactured as single, integrated parts, eliminate the need for assembly and increase the durability of robotic components. Compliant joints within these mechanisms enable movement through elastic deformation of the part itself, enhancing their robustness and reducing the need for maintenance.

Non-planar AM further contributes to this field by allowing 3D layer paths, minimising the staircase effect and enhancing the surface quality and practical performances.

First, this thesis provides a detailed review of the current state of monolithic mechanisms with compliant joints and the advances in non-planar additive manufacturing.

In pursuit of practical applications, this work presents the design and development of two additively manufactured monolithic robotic components: a compliant joint gripper and a robot with delta kinematics. These designs showcase the benefits of AM in producing simple, efficient, and lightweight components tailored for industrial applications.

Furthermore, the thesis introduces an innovative slicing algorithm for non-planar AM designed for desktop machines. This new slicing methodology optimises layer orientation along curved paths, improving part surface finish through slices from the intersection with the model to be printed to accurately reproduce the model top surfaces while avoiding collisions.

By integrating advanced design and manufacturing techniques, this thesis demonstrates AM's transformative impact on robotic design, potentially redefining standards in high-performance, customised parts in robotic and industrial fields.

Table of contents

List of figures

List of tables

Nomenclature

Acronyms / Abbreviations

ABS Acrylonitrile butadiene styrene

AM Additive manufacturing

DMLS Direct meta laser sintering

MEX Material extrusion

PBF Powder bed fusion

PETG Polyethylene terephtalate glycol

PLA Polylactic acid

PLG Push-latch gripper

SLA Stereolitography

TPU Thermoplastic polyuretane

Chapter 1

Motivation

1.1 Additive Manufacturing Technologies

Additive Manufacturing (AM), commonly known as 3D printing, represents a transformative approach to industrial production that has significantly evolved over the past few decades. Unlike traditional subtractive manufacturing processes, which remove material from a solid block to create an object, additive manufacturing builds objects layer by layer from the bottom up, using materials such as plastics, metals, ceramics, and composites. This layer-by-layer construction allows for creating complex geometries that would be difficult, if not impossible, to achieve with conventional methods.

Several key technologies fall under the umbrella of additive manufacturing, each with unique strengths and applications. These include Stereolithography (SLA), Powder Bed Fusion (PBF), Material Extrusion (MEX), and Direct Metal Laser Sintering (DMLS), among others. SLA uses a laser to cure liquid resin into hardened plastic, making it ideal for producing highly detailed prototypes and patterns. On the other hand, PBF uses a laser to sinter powdered material, creating durable and functional parts without the need for support structures. MEX, one of the most widely used techniques, extrudes thermoplastic filaments to build parts, making it accessible and versatile for various applications. DMLS focuses on metal powders, producing robust and complex metal parts crucial for industries like aerospace and medical implants.

The importance of additive manufacturing has grown exponentially due to its ability to produce prototypes rapidly, customise products to individual specifications, and reduce waste by using only the necessary material. This technological advancement has revolutionised the aerospace, automotive, healthcare, and consumer goods industries. In aerospace, for example, AM enables the production of lightweight, high-strength components that improve

fuel efficiency and performance. In healthcare, it allows for creating patient-specific implants and prosthetics, enhancing treatment outcomes.

In summary, additive manufacturing has expanded the possibilities for design and production and has become an integral part of modern manufacturing strategies. Its continuous development promises further innovations and efficiencies, cementing its role as a cornerstone of the future of manufacturing.

Since MEX and PBF are the technologies of interest for this thesis, they will be further discussed in the following sections.

1.1.1 Material Extrusion

In this process, a thermoplastic filament is fed into a heated extruder, where it is melted and then deposited layer by layer onto a build platform. The materials used in MEX are primarily thermoplastic polymers, chosen for their ability to be repeatedly melted and solidified. Common materials include Polylactic Acid (PLA), known for its biodegradability and ease of printing; Acrylonitrile Butadiene Styrene (ABS), valued for its durability and toughness; and Polyethylene Terephthalate Glycol (PETG), which combines the ease of printing of PLA with the strength of ABS. Other materials like Nylon and Thermoplastic Polyurethane (TPU) offer unique properties such as flexibility, strength, and elasticity, expanding the range of possible applications.

In recent years, the use of composite materials in MEX has gained significant traction. Composite filaments typically consist of a thermoplastic matrix embedded with reinforcing fibers such as carbon, glass, or even metal particles. These materials enhance the mechanical properties of the printed components, offering improved strength, stiffness, and thermal resistance compared to standard thermoplastics. The development of MEX for composites has expanded the range of applications, particularly in industries where material performance is critical, such as aerospace and automotive sectors.

The primary components of a Material Extrusion system include the extrusion head (or print head), the build platform, and the material feed mechanism. The extrusion head comprises a nozzle through which the material is deposited, a heating element to melt the filament, and a drive system that controls the flow rate of the material. The build platform serves as the base upon which the object is constructed; it often includes a heating system to maintain optimal adhesion of the first few layers. The material feed mechanism is responsible for transporting the filament from the spool to the extrusion head, often incorporating a stepper motor for precise control of the material feed rate.

Material Extrusion is also suitable for the production of composite parts. These are a combination of two materials with different physical and chemical properties that interact synergically to obtain an object with desired characteristics. Composite parts are composed of a matrix, which is the material that protects the reinforcement, which is the material that gives the structural strength to the part. Often, the reinforcements are fibres, which are also adopted in MEX. Usually, the fibre is enveloped by a polymer matrix; as a consequence, additional considerations include the management of the reinforcing fibres within the filament to ensure even distribution and prevent nozzle clogging. The alignment of these fibres during extrusion is also crucial, as it influences the mechanical properties of the final part. Advanced MEX systems may include dual extrusion capabilities, enabling the simultaneous deposition of two different materials or combining a composite material with a support structure, facilitating the creation of complex geometries. Fig. 1.1 schematises the presented process.

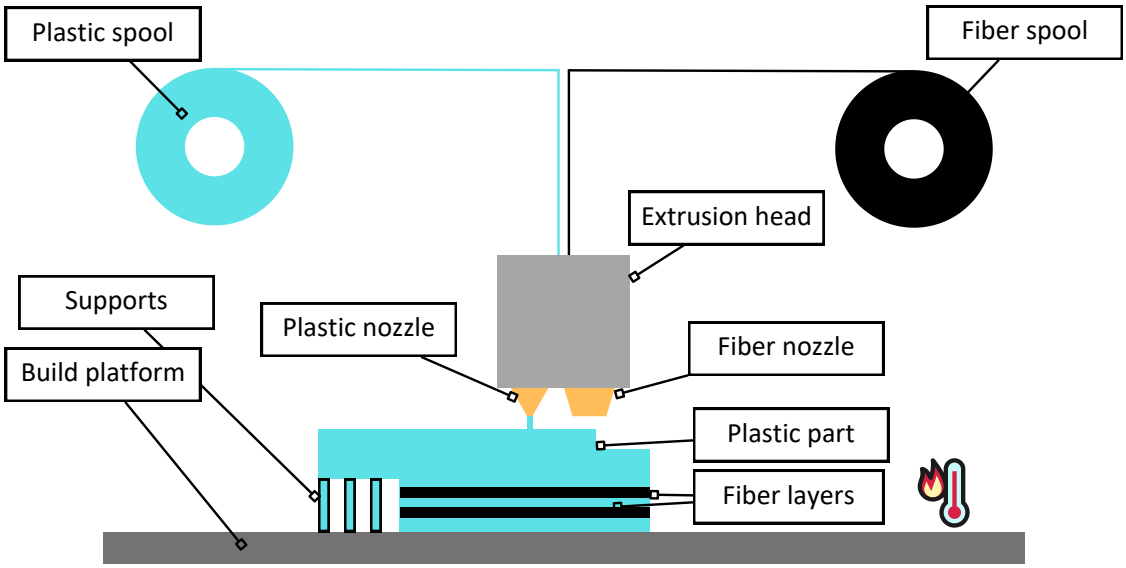

Figure 1.1 MEX process

1.1.2 Powder Bed Fusion

Powder Bed Fusion (PBF) is an advanced additive manufacturing technique that has revolutionized the field of rapid prototyping and manufacturing. This process relies on the principles of melting and laser technology to create three-dimensional objects from powdered materials, typically plastics, metals, or ceramics.

The actual manufacturing process occurs within a specialised chamber of the PBF machine, which is filled with a bed of fine powder of the chosen material. The powder is evenly distributed across the build platform in a thin layer by a roller or a blade. A high-powered laser then selectively fuses the powder particles by scanning the surface layer according to the cross-sectional data of the 3D model. As the laser moves across the powder bed, it raises the temperature of the powder just above its melting point, causing the particles to fuse without fully liquefying. This melting process solidifies the material in the desired shape of the cross-section. Once a layer is completed, the build platform lowers slightly, and a new layer of powder is spread over the previous one. The laser then sinters the next cross-section of the model on top of the last layer. This process repeats layer by layer until the entire object is formed. Fig. 1.2 schematises the presented process.

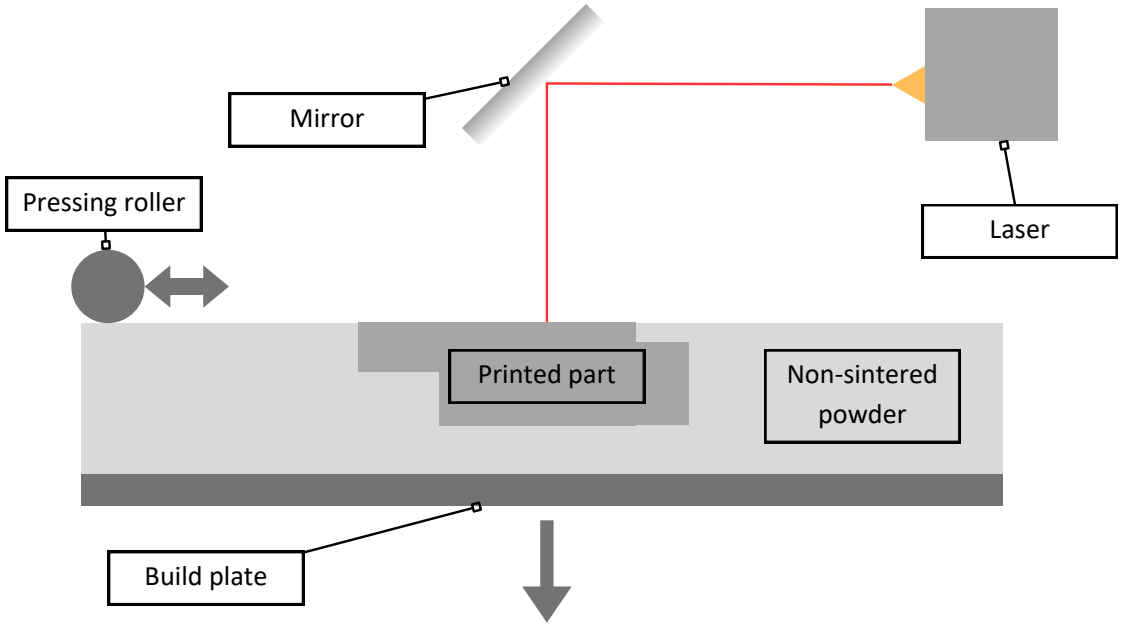

Figure 1.2 PBF process

Since the unsintered powder surrounding the object supports it during the build process, there is no need for additional support structures, which are often required in other additive manufacturing techniques such as stereolithography (SLA) or material extrusion (MEX). After the printing process is complete, the object can cool down within the powder bed to minimise warping and internal stresses. The final step involves extracting the object from the powder bed and removing any loose, unsintered powder. This leftover powder can often be recycled for future builds, making PBF a relatively material-efficient process.

Powder Bed Fusion offers several benefits, including high precision, good mechanical properties of the final parts, and a wide range of material compatibility. It is widely used in various industries, from aerospace and automotive to healthcare and consumer goods, for producing functional prototypes, end-use parts, and complex components with high-performance requirements. Overall, the PBF process embodies a sophisticated interplay of digital design, material science, and laser technology, underscoring its significant role in advancing modern manufacturing techniques.

1.2 How Can AM be advantageous?

The advent of additive manufacturing technologies has ushered in a new era of manufacturing, bringing with it a host of advantages that are revolutionising how we design and produce objects. One of the most transformative aspects of AM is its capability to create monolithic mechanisms and the innovative approach of non-planar printing, both of which offer substantial benefits over traditional manufacturing methods. In the following sections, these approaches will be further discussed.

1.2.1 Monolithic Mechanisms with Compliant Joints

Monolithic mechanisms are systems that can be employed immediately after production. On the other hand, compliant joints are elements that achieve motion transmission through the deformation of one or several elastic bodies. Integrating additive manufacturing technologies in producing monolithic mechanisms with compliant joints brings many advantages, making it an increasingly attractive option for various engineering applications. These benefits stem from the unique capabilities of AM processes and the inherent strengths of monolithic and flexural designs.

One of the primary advantages of monolithic mechanisms is the significant reduction in assembly complexity. Since these mechanisms are fabricated as single, continuous pieces, the need for assembling individual parts is eliminated. This translates to lower labor costs, reduced assembly time, and a substantial decrease in the likelihood of assembly errors. Additionally, the absence of joints and fasteners, which are typically required in traditional mechanisms, leads to improved reliability and durability. This seamless construction enhances the structural integrity of the mechanisms, allowing them to withstand higher loads and stresses, thus reducing the risk of failure due to fatigue at joints. As a result, the monolithic mechanisms exhibit high repeatability in their motion, which is crucial for

applications requiring consistent performance. Furthermore, the continuous nature of these structures eliminates weak points, enhancing their overall strength and durability.

Moreover, monolithic mechanisms can be designed to minimize material usage without compromising strength and functionality, leading to significant weight reductions. This advantage is particularly important in aerospace and robotics applications, where lower weight contributes to improved efficiency, reduced energy consumption, and enhanced manoeuvrability. The reduction in weight does not come at the cost of mechanical performance, thanks to the precise control over material distribution that additive manufacturing offers. Since the need for assembly operations, fasteners, and bearings is limited, logistic simplification occurs.

Another critical advantage is the elimination of lubrication and maintenance. Compliant joints operate based on elastic deformation rather than sliding or rolling contact, negating the need for lubrication. This results in maintenance-free operation and reduces the risk of contamination in sensitive environments. Compliant joints are also unaffected by stick-slip friction and, thus, tend to behave more predictably. Additionally, the absence of wear and tear associated with traditional joints extends the lifespan of the mechanism, further enhancing its reliability and durability.

The versatility of additive manufacturing also allows for the integration of multiple functionalities into a single monolithic mechanism. Components can be designed to include not only mechanical functions but also embedded sensors, actuators, or fluidic channels. This integration reduces the need for additional components and simplifies the overall system design, leading to more compact and efficient solutions.

From an economic perspective, AM could be particularly cost-effective for low-volume production runs or custom parts, where traditional manufacturing methods would incur high setup costs. The ability to print complex monolithic mechanisms on demand without the need for expensive moulds or tooling makes it an attractive option for prototyping and small-scale production. The rapid nature of additive manufacturing technologies enables quick prototyping and iteration, allowing designers to move from digital models to physical prototypes swiftly. This accelerates the development cycle, facilitating faster design testing, validation, and refinement, thereby enhancing innovation and reducing time-to-market.

In conclusion, adopting monolithic mechanisms with compliant joints printed through AM technologies offers a comprehensive suite of advantages, including reduced assembly complexity, enhanced precision, improved structural integrity, and greater design freedom. These benefits, coupled with the cost-effectiveness and rapid prototyping capabilities, make these mechanisms a compelling choice for advanced engineering applications. The synergy

of these advantages underscores the transformative impact of additive manufacturing on modern manufacturing and product development. 1.3 summarises the previous presented advantages.

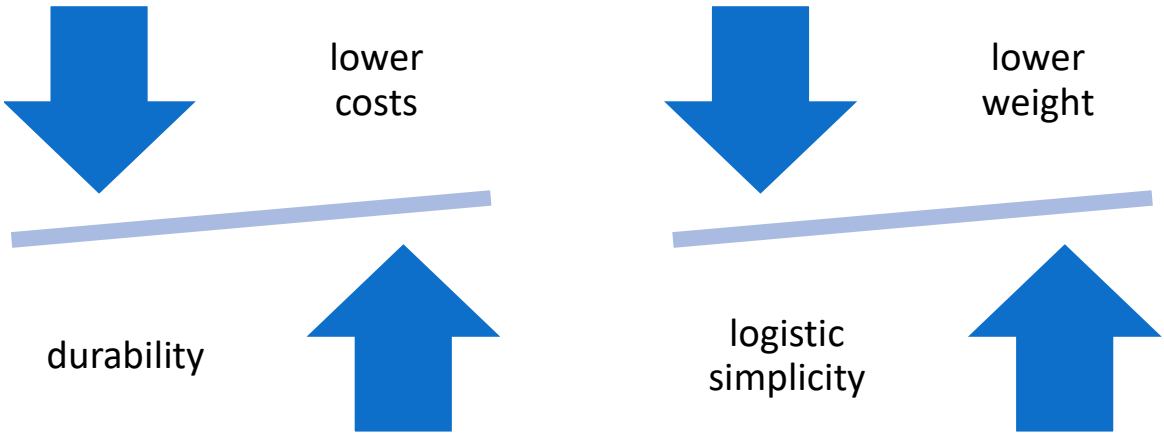

Figure 1.3 Advantages of monolithic mechanisms

1.2.2 Non-planar MEX

Non-planar MEX represents a significant advancement in additive manufacturing, offering numerous benefits that extend beyond traditional layer-by-layer planar techniques. Traditional material extrusion can be defined as a 2.5D process since the object is constructed one layer at a time. Each layer is essentially a two-dimensional slice of the final object. The extrusion nozzle moves in the x-y plane to deposit material, creating a flat layer. Once a layer is completed, the nozzle moves up (or the build platform typically moves down) in the z-axis to allow for the next layer to be deposited, as shown in 1.4.

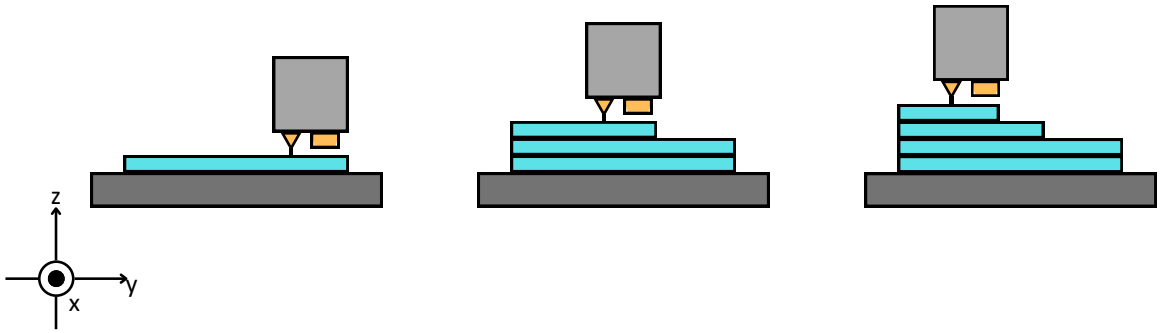

Figure 1.4 2.5D MEX process

This sequential stacking gives the impression of a third dimension, but since each step involves 2D motion, it's considered a 2.5D process. Often, the result is a staircase effect on inclined and curved surfaces, characterised by visible layer lines and a rough finish, necessitating post-processing steps such as sanding, polishing, or chemical smoothing to achieve the desired surface quality.

Non-planar MEX, instead, involves actual 3D movements, characterised by simultaneous x-y-z movements, as shown in 1.5.

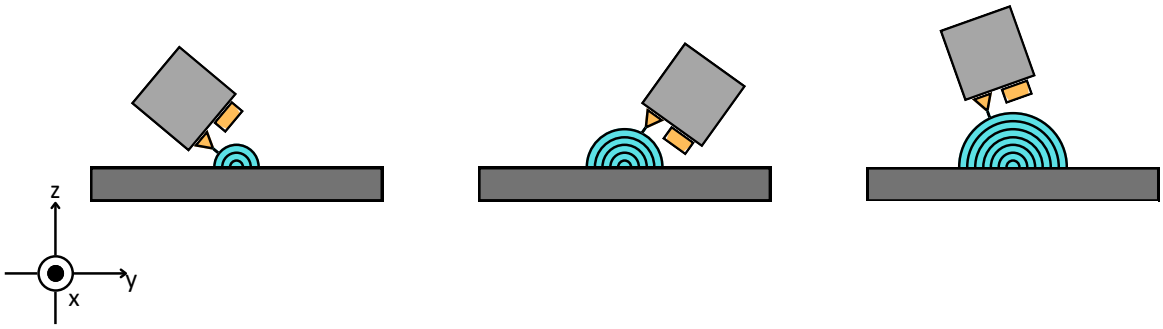

Figure 1.5 3D MEX process

The primary advantage of this process is that it eliminates the typical aesthetic defects in horizontal regions with low curvature (a.k.a "staircase effect"). As a result, parts are characterised by a much smoother surface directly from the printer, minimising or negating the need for extensive post-processing.

The enhanced surface finish provided by non-planar 3D printing offers several practical benefits in industrial contexts. Firstly, it improves the aesthetic appeal of the printed parts, which is crucial for consumer products where visual quality is a key selling point. A smoother surface finish also enhances the tactile experience, making products more pleasant to touch and handle. This is particularly important in automotive, aerospace, and consumer electronics industries, where visual and tactile quality are fundamental.

In addition to aesthetic and tactile improvements, the superior surface finish achieved through non-planar MEX has functional benefits. For instance, smoother surfaces can reduce friction and wear in mechanical components, leading to longer lifespan and better performance. This is especially relevant in applications involving moving parts or components that interact with other surfaces, such as gears, bearings, and seals. In the medical field, smoother surfaces on implants and prosthetics can reduce the risk of tissue irritation and improve biocompatibility.

Another significant feature of non-planar material extrusion is the potential for enhanced mechanical properties. Printing along curved paths allows the distribution of the material

and the alignment of it to the principal directions of stress. This can improve the distribution of stresses and reduce weaknesses associated with layer adhesion. Parts may be stronger and more durable than those produced with traditional planar methods. The ability to tailor the orientation and path of material deposition also allows for optimization of mechanical properties in specific areas of the part, further enhancing performance.

From an industrial perspective, the reduction in post-processing requirements provided by non-planar MEX translates to significant cost and time savings. Post-processing can be labour-intensive and time-consuming, often involving multiple steps and specialized equipment. By minimising the need for these additional processes, non-planar material extrusion streamlines the production workflow, reduces labour costs, and accelerates time-to-market. This efficiency is particularly beneficial for industries that operate on tight production schedules and high-volume manufacturing.

Moreover, the improved surface finish and mechanical properties of non-planar manufactured parts can expand the range of applications for additive manufacturing. High-quality surface finishes and optimized mechanical performance open up new possibilities in aerospace, automotive, and healthcare industries, where stringent standards and demanding conditions must be met. The ability to produce complex geometries with excellent surface quality and robust mechanical properties makes this process a versatile and powerful tool in the industrial manufacturing landscape.

1.3 Thesis Objectives

The main objectives can be listed as follows:

1. **Investigating the state-of-the-art:**

   To study and investigate the state-of-the-art of non-planar MEX and the adoption of AM for monolithic mechanisms production.

2. **Showing new possibilities and applications of AM:**

   To analyse how AM can expand the industrial's horizon.

3. **Showing new modalities of design:**

   To exhibit different paradigms in the design of parts.

4. **Test and develop:**

   To test and analyse the proposed systems.

1.4 Thesis Layout

This dissertation is focused on showing how AM can be a technology capable of expanding the industrial scenario. This expansion is shown in relation to two sub-projects: the design of monolithic mechanisms that employ compliant joints and the development of an innovative slicer to produce parts through non-planar MEX. This thesis is structured as follows:

1. **Part I: Literature review on compliant and monolithic mechanisms production through AM and on non-planar MEX**

   The relevant literature around non-planar MEX and monolithic mechanisms; a short review of gripper's and delta robots' literature will be presented.

2. **Design of monolithic mechanisms with compliant joints**

   The design and development of two monolithic mechanisms will be presented.

3. **Part III: Part production through Non-Planar MEX**

   This chapter will present a novel algorithm capable of performing non-planar MEX for desktop additive manufacturing machines.

4. **Part IV: Conclusions**

Part I

Literature review on compliant and monolithic mechanisms production through AM and on non-planar MEX

Chapter 2

State of the art

2.1 Background

This chapter presents a review of the literature pertinent to this thesis. As outlined in the previous chapter, the two primary areas of focus are monolithic and compliant mechanisms and non-planar MEX. It is important to examine the current state of the art of grippers and delta robot architectures, as the next part will also address the design and validation of both a monolithic gripper and a monolithic delta robot. At the end of the chapter, the relevant literature on non-planar MEX is presented.

2.2 Relevant robotic systems

This section briefly presents the literature review related to robotic grippers and delta robot systems.

2.2.1 Robotic grippers

The grasping process plays a fundamental role in industrial automation, where it is typically addressed through the use of robotic grippers. The scientific literature in this domain is vast and cannot be thoroughly reviewed in this thesis.

The actuation system is arguably the most effective criterion for classifying robotic grippers, which can be categorized as electric, pneumatic, hydraulic, vacuum-based, or magnetic. Among these, electric and pneumatic grippers dominate industrial automation applications (Birglen and Schlicht (2018)). Beyond these well-established solutions, the

gripper literature includes numerous innovative and unconventional designs, as exemplified in works such as Petterson et al. (2010).

Concurrently, soft robotic grippers—devices constructed from highly deformable materials with Young's modulus comparable to biological tissues—constitute another class of systems with unique properties. An early example of this approach is the pneumatic soft three-fingered gripper by Muscato et al. (2005). More recently, Deimel and Brock (2013) introduced the *Pneuflex* design, which was released as open-source to facilitate experimental replication. Traditionally, the fabrication of highly deformable parts relied on silicone molding; however, advances in AM have enabled alternative production methods. For instance, Drotman et al. (2017) and Ge et al. (2018) utilized a Stratasys Connex multi-material 3D printer and a Digital Light Processing (DLP) printer, respectively, to fabricate soft pneumatic actuators. Other grippers whose development significantly leveraged AM have been made available as open-source designs by the Yale OpenHand Project Ma and Dollar (2017). Specifically, several models developed by Ma et al. (2015) employ the Hybrid Deposition Manufacturing (HDM) method to produce soft, multi-fingered, underactuated robotic hands with rubber-like flexures featuring programmable stiffness. Furthermore, another category of unconventional soft grippers operates by conforming to the object to be grasped. Examples include the work by Brown et al. (2010), which introduced granular material jamming; Chen et al. (2021), who presented an extensible origami gripper; and Tsugami and Nishida (2017), who developed a soft magnetically actuated end-effector. Another category of grippers is related to passive actuation. Kodnongbua et al. (2022) introduced a computational design methodology for robotic end-effectors, specifically targeting passive configurations. Seino et al. (2024) propose a Passive Actuator-Less Gripper (PALGRIP) for picking a piece of fabric from a stack of fabric parts and placing the picked part.

2.2.2 Delta robot architectures

The Delta robot, introduced by Clavel in the 1980s (Clavel (1987)), is one of the most extensively studied and widely used parallel manipulators. It consists of three actuators mounted on its base, which drive three parallel arms connected to an end-effector platform. The kinematic chains restrict the motion of the platform to three translational degrees of freedom. The Delta robot is well-known for its lightweight structure, high speed, and precision, which make it particularly suitable for packaging and pick-and-place tasks (Staicu (2019)). Its versatile and adaptable design has enabled its continued application in various innovative domains across multiple industries. Several recent studies showcase the diverse

applications of the Delta robot. For instance, Do et al. (2021) integrated an image processor with a Delta robot to classify products and quickly pick and drop them into a classification box. Similarly, Xiao et al. (2022) utilized a Delta robot in a robot-assisted retinal surgery system. Okunevich et al. (2021) developed the DeltaCharger, a system based on Delta kinematics, capable of precisely positioning a set of electrodes to transfer energy between two robots. Hirano et al. (2014) created a Delta robot driven by pneumatic artificial muscles, proposing its potential as a rehabilitation and VR/AR haptic device.

2.3 Compliant and monolithic mechanism

It is noteworthy that compliant mechanisms are also employed in several applications. Compliant mechanisms, that replace traditional joints with flexible components such as flexure hinges or elastic bearings, have been the subject of extensive research over the last two decades. Howell (2001), Howell et al. (2013) and Lobontiu (2001) works provide thorough overviews of compliant mechanisms, covering design strategies, guidelines, and practical examples of their use.

Regarding the gripper design, various compliant have also been explored. Among compliant designs, Wang et al. (2020) applied a topology optimization framework to develop a 2-degree-of-freedom (2DOF) compliant gripper. Meanwhile, McGowan and Hao (2022) devised a morphing compliant mechanism capable of both gripping and retraction modes, utilizing a single actuator to achieve comparable performance in both functions. Hsiao et al. (2022) proposed compliant bistable grippers designed for passive perching applications in UAVs. Kargar and Berselli (2024) present the design, analysis, and optimisation of TriCoM, a portable three-finger underactuated gripper with compliant joints designed for food and fruit handling.

Baggetta et al. (2023) introduce an underactuated prosthetic hand designed to provide a cost-effective, functional, and human-like solution for individuals with upper limb amputations. The design features compliant spring-based hinges and a motor decoupling mechanism, enhancing natural movement and adaptability to various objects.

In the context of robotic mechanisms, substantial ranges of motion are typically required, and achieving these using compliant mechanisms can be challenging. This is because large motion ranges necessitate considerable joint deformations, which in turn can negatively impact the durability and robustness of the system. Consequently, it is crucial to examine the solutions proposed in the literature to address this challenge.

Among the first compliant parallel robots, Raatz et al. (2004) introduced a macro-scale parallel robot that substitutes conventional bearings with pseudo-elastic flexure hinges. This robot features a spatial parallel structure with three translational degrees of freedom, driven by three linear direct-drive actuators. The symmetrical structure, combined with the optimized design of the flexure hinges, contributes to its high stiffness, with experimental repeatability below $0.3[\mu m]$.

The work by Correa et al. (2016) is particularly significant as it presents one of the first comprehensive applications of compliant joints in parallel robots, fabricated using the printed circuit MEMS (PC-MEMS) technique Sreetharan et al. (2012). Specifically, their approach involves using two-dimensional manufacturing techniques, such as sheet-metal processing and laser cutting, to fabricate a laminated Delta robot with prismatic actuation. The robot is bent out of the plane to achieve a three-dimensional shape. This manufacturing process is simple and cost-effective, making it ideal for use in open-source hardware projects focused on creating low-cost, complex electromechanical systems.

The same methodology was later adopted by Mcclintock et al. (2018), who developed the milliDelta, also utilizing the PC-MEMS technique at the millimeter scale. The authors demonstrated that the milliDelta system is capable of precise motion control of the payload relative to the workspace.

The team led by Mannam et al. at Carnegie Mellon University (CMU) (Mannam et al. (2021a)) introduced a compliant Delta manipulator built with 3D printing and soft materials. The parallelogram links in the design of this Delta robot were optimized by varying twelve dimensional parameters and using two different materials. The resulting mechanisms were tested for stiffness by displacing them and measuring the resulting forces and rotation angles, with the best combinations achieving near-delta behavior. This approach was subsequently applied in Mannam et al. (2021b) to create a low-cost, 3D-printed, compliant gripper consisting of two centimeter-scale 3-DOF Delta robots actuated by off-the-shelf linear actuators. Additionally, the authors introduced the DeltaZ robot Patil et al. (2022), a low-cost, centimeter-scale Delta-style robot that is easy to assemble, maintain, and afford.

Although the works by Correa et al., McClintock et al., and Mannam et al. are commendable, their focus was primarily on small-scale systems, and only a few large-scale implementations have been reported thus far. As a result, the fabrication of compliant robots at larger scales remains an unresolved challenge.

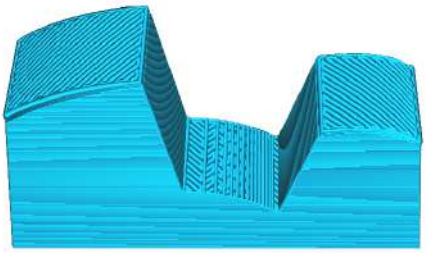

Figure 2.1 The two-towers model. The approach of Ahlers et al. (2019) used in this Figure cannot curve the middle part as it would produce collisions during printing. The result of our approach follows all surfaces, with curved layers throughout the part as shown in Figure 5.2.

2.4 Non-Planar MEX

Early studies (Allen and Trask (2015); Chakraborty et al. (2008)) demonstrated that 3-axis printers are capable of reproducing curved surfaces using commercially available equipment. This initial work paved the way for the development of algorithms designed to automatically generate non-planar layers:

Song et al. (2016) introduced a method that varies the toolpath heights on the top layers, adjusting their top surfaces up or down to more accurately reflect the true surface geometry—similar to the concept of anti-aliasing in Computer Graphics. This approach requires splitting and sequencing the paths to minimize nozzle gouging, along with meticulous flow management to account for the varying deposition thicknesses along each path.

Ezair et al. (2018) proposed extracting layers as iso-surfaces from a user-defined trivariate parameterization, ensuring uniform spacing between them. A similar method generates a dense set of toolpaths for each layer. Any resulting collisions are addressed in a post-processing step, which involves splitting and ordering the toolpaths to avoid interference.

Ahlers et al. (2019) developed an algorithm that curves the accessible top layers of a print, while the inner part remains printed using standard planar layers. Curving only the top layers necessitates precise stitching with the surrounding flat layers. Any surfaces that could potentially be curved but would lead to collisions during printing are excluded. This approach becomes problematic when top surfaces are positioned at heights where one surface obstructs access to another.

The method proposed by Etienne et al. (2019) focuses on optimizing a continuous deformation of the entire input model's *volume*. The goal is to flatten the top surfaces while making others steeper. The flattening process results in curved surfaces, whereas steepening enhances the slicing quality of other surfaces, effectively enabling adaptive

slicing as a secondary outcome. The deformed model is then sliced into flat layers, and the resulting toolpaths are mapped back to their original positions, creating non-planar toolpaths with varying thicknesses across the part. The deformation is subject to constraints that ensure (optional) minimum and maximum thickness limits and prevent collisions. Once this mapping is achieved, the layers are guaranteed to be free from collisions globally, eliminating the need for explicit collision detection checks. While the method is very general and can curve surfaces throughout the part, it suffer a major downside: a discretization of the entire build volume by tetrahedrization. This makes the overall approach computationally heavy, especially as it iterates solving a large least-square problem under linear inequality constraints.

These techniques introduce important ideas for our purpose. A conical nozzle collision model Ahlers et al. (2019); Etienne et al. (2019); Ezair et al. (2018) leads to the observation that surfaces with an angle everywhere below a critical angle can be printed without self-collisions Ahlers et al. (2019). This is used to detect collisions Ahlers et al. (2019); Ezair et al. (2018), identify compatible top surfaces Ahlers et al. (2019); Etienne et al. (2019), and to constrain deformation gradients Etienne et al. (2019). Nozzle gouging and the influence of the path orientation with respect to the slope are identified as important issues Ahlers et al. (2019); Allen and Trask (2015); Chakraborty et al. (2008); Song et al. (2016), even though not directly addressed.

Furthermore, most existing methods create toolpaths using strategies designed for planar layers, where the curved layers are often derived by deforming toolpaths from flat layers Ahlers et al. (2019); Etienne et al. (2019); Song et al. (2016).

2.5 Curved Printing with Multi-Axis Machines

The previously discussed methods primarily focus on 3-axis machines. However, to achieve greater flexibility and allow the nozzle to tilt and follow surface contours more effectively, another area of research emphasizes multi-axis systems. Examples include multi-degree-of-freedom (DOF) extrusion devices (e.g.,G et al. (2023); Huss and Erdman (2023)) and robotic arms (e.g.,Lettori et al. (2024); Zhang et al. (2022)).

Non-planar printing with multi-axis machines enhances several aspects of printed parts, such as reducing the need for support materials Dai et al. (2018); Hong et al. (2022); Lau et al. (2023); Liu et al. (2024), increasing structural integrity Bi et al. (2023); Guidetti et al. (2023); Pérez-Castillo et al. (2023); Shan et al. (2023), and addressing multiple objectives simultaneously Zhang et al. (2022). Combining these techniques with fiber extrusion can

further significantly enhance part strength Akhoundi et al. (2024), Fang et al. (2024), Kipping and Schüppstuhl (2023), Palmer and Laliberte (2023), Zhao et al. (2023), Zhang et al. (2024).

For a comprehensive overview of the latest advancements in non-planar printing, including multi-axis additive manufacturing, the review by Tang et al. (2024) is recommended.

Part II

Design of monolithic mechanisms with compliant joints

Chapter 3

Proposed Push-Latch Gripper

3.1 Contribution

In this chapter the design, fabrication, and validation of a "passive" monolithic gripper, manufactured through additive manufacturing (AM) is discussed; its operation relies on a push-latch mechanism hereafter referred to as the Push-Latch Gripper (PLG). Push-latch mechanisms are widely used across various engineering fields (e.g., SD card insertion/ejection slots, furniture closures, etc.). While several implementations have been described in both scientific and patent literature (see King and Levey (2010); Louis (2003); Nishimura (1988) for examples), to the best of the author's knowledge, this work represents one of the first applications of such mechanisms in the design of robotic grippers.

The operating principle of the PLG is illustrated in Fig. 3.1: *i)* the gripper first approaches the object to be grasped; *ii)* when the object makes contact with the base of the gripper, additional pushing causes the compliant fingers to close; *iii)* once a specific threshold is reached, the gripper's fingers lock in place; *iv)* the grasped object can then be securely manipulated and transported; *v)* finally, an additional push is required to release the object. As the gripper's actuation is achieved by moving it (e.g., using a robotic manipulator), the PLG is entirely passive and does not require any external power source. This type of solution is not widely used in practice, possibly due to its limited adaptability. However, industrial pick-and-place operations typically do not require high levels of flexibility or adaptability, making grippers such as the PLG well-suited for these contexts.

Additionally, the gripper described in this thesis features several noteworthy characteristics:

- It is produced through AM, enabling rapid design iterations and greater design freedom compared to conventional manufacturing processes Su et al. (2012). Commercial grippers

(e.g., those by Festo, Schunk, or BTM) are typically made of metallic materials and often require the integration of complex onboard systems or electronics, or pneumatic lines. In contrast, the PLG is made from polymeric materials and does not necessitate onboard drive systems, resulting in reduced gripper weight.

- Traditional grippers are composed of multiple assembled components, whereas the device presented here is monolithic Lussenburg et al. (2021a), requiring no assembly. This feature allows the gripper to be deployed immediately after fabrication, leading to significant time and cost savings. Furthermore, as precise mating of parts is unnecessary, fabrication processes with looser tolerances (and thus lower costs) can be utilised. Finally, since no additional components (e.g., fasteners, bearings, etc.) are needed, monolithic systems often outperform their traditional counterparts in terms of weight.
- Another distinctive feature of this design is the use of compliant joints instead of traditional rotational joints. Unlike conventional kinematic pairs, compliant joints offer greater predictability and durability due to their resistance to wear, albeit at the expense of reduced motion ranges. Additionally, compliant joints are not subject to stick-slip friction, enhancing their predictability. This design approach is particularly compatible with AM technologies, as evidenced by numerous examples in the literature Bruyas et al. (2015); Fowler et al. (2014); Hsiao et al. (2022); Kiener et al. (2019).

In summary, the contributions of this activity are as follows: *i)* introduction of a novel gripper design concept; *ii)* description of an efficient computational method to virtually evaluate the PLG's performance prior to physical prototyping; *iii)* experimental validation of the PLG.

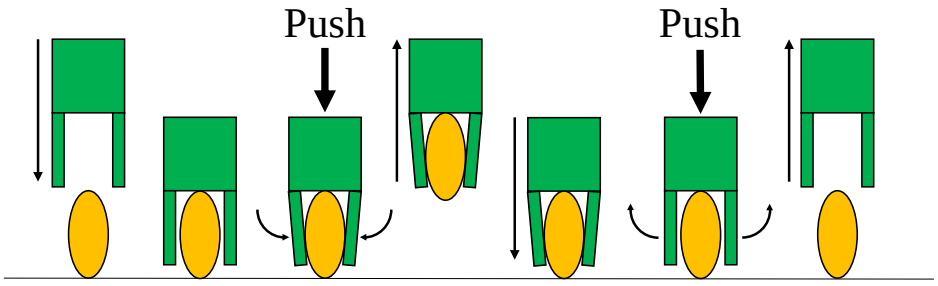

Figure 3.1 Schematic operation of the proposed push-latch mechanism gripper.

3.2 Design of the System

3.2.1 System Description

The Push-Latch Gripper (PLG) consists of two opposing fingers and, in the configuration presented in this thesis, is designed to grasp objects with two parallel, flat faces. When the gripper is pressed against the workpiece, the fingers move toward the object and contact its sides. This movement is achieved through the kinematic structure described in the subsequent sections. Figure 3.2 illustrates the sequence of phases involved in this process.

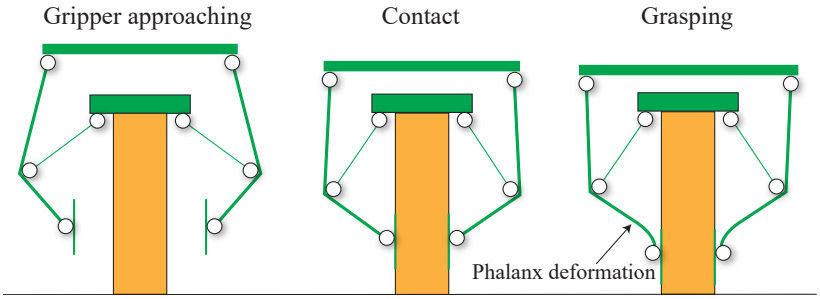

Figure 3.2 Grasp sequence. The diagram illustrates the behaviour of the gripper mechanism during the three main phases of the grasping sequence.

The gripper supports two primary grasping approaches: *force closure* (relying on friction) and *form closure*. These modalities are depicted in Figure 3.3.

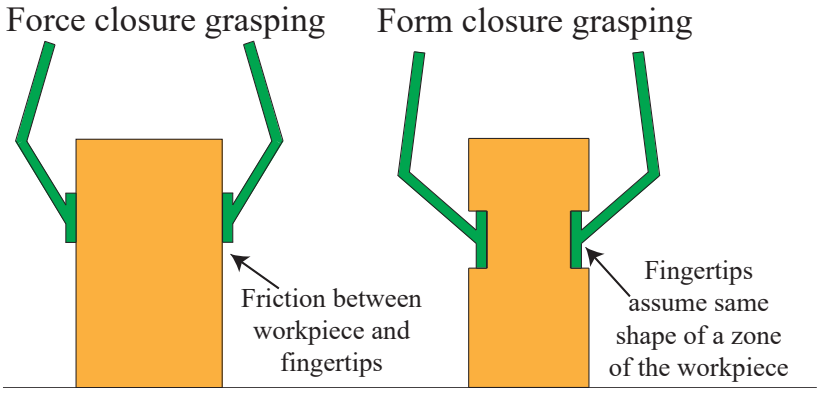

Figure 3.3 Grasping modalities. The diagram shows the PLG's force closure (left) and form closure (right) grasping techniques.

In the force closure mode, the contact forces must be sufficiently high to lift and manipulate the object. To achieve this, the friction generated by the contact between the fingers and the workpiece must exceed the weight of the object.

In the form closure mode, the fingertips can be customised to geometrically match the shape of the object to be grasped. Additive Manufacturing (AM) significantly facilitates this approach, enabling the design of complex, tailored geometries.

In both grasping modes, the motion of the gripper is initiated when it presses against the workpiece. This causes the platform—constrained by a linear guide—to activate the fingers. The fingers' movement, in turn, drives a pin that slides within a cam mechanism. When the pin reaches a specified position, the fingers lock in place. An additional push releases the mechanism, allowing the fingers to open.

As highlighted in this thesis, the fingertips of the PLG can be tailored to handle objects with non-planar geometries, making the system adaptable to various applications. However, its passive design limits its ability to grasp objects with highly variable shapes. Nonetheless, this limitation is acceptable in structured industrial environments, where the PLG's low cost and simplicity make it an attractive option. Figure 3.4 presents the physical prototype of the PLG along with the nomenclature of its main components, while Figure 3.5 illustrates the complete grasping sequence.

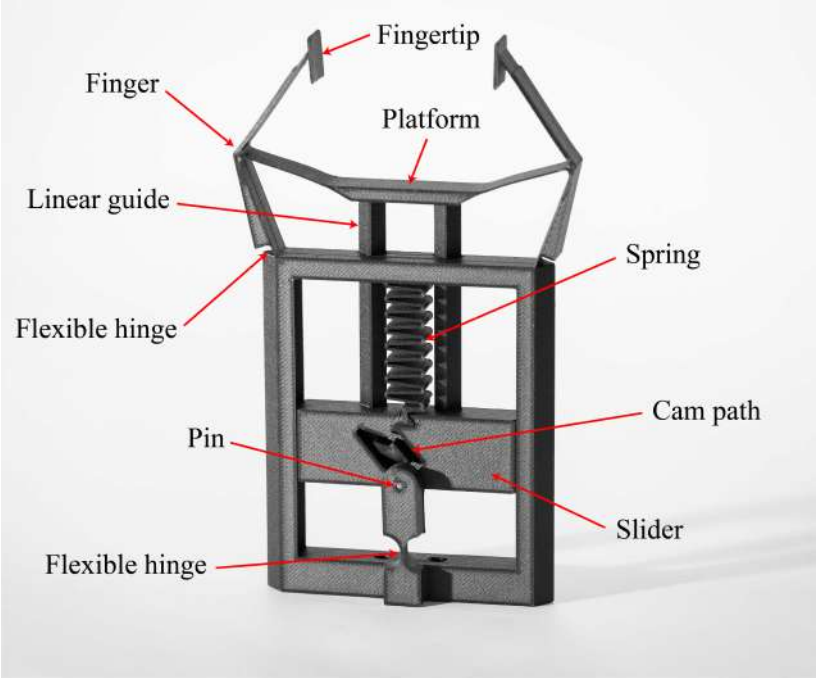

Figure 3.4 PLG physical prototype (with nomenclature).

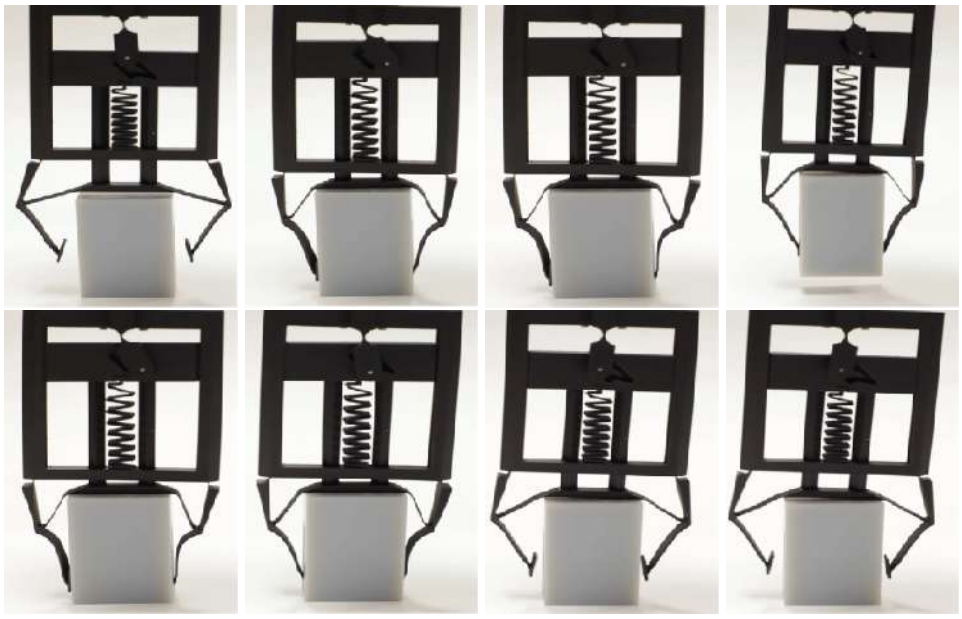

Figure 3.5 Grasping sequence.

3.2.2 Finger Kinematics

The kinematic model underlying the finger design is presented in Figure 3.6. Due to the system's symmetry, only one side of the mechanism is shown, including three moving bodies and the frame. The first body includes segments of lengths l_2 and l_4, rigidly connected at a fixed angle γ. The segment l_2 is initially positioned at an angle θ_2 relative to the horizontal axis.

A rod of length l_3 connects the first body to the moving platform, which applies the pressing force. The mechanism has a single degree of freedom (DOF): as the platform moves downwards, the terminal portion of the finger approaches the symmetry axis.

The relationship between θ_2 and the vertical position y_B is defined by:

$$y_B = -l_2 \sin(\theta_2) + \sqrt{l_3^2 - (l_2 \cos(\theta_2) - l_1)^2} \tag{3.1}$$

The horizontal position of the contact plates, x_C, is linked to θ_2 via:

$$\theta_2 = 2 \arctan\left(-\frac{-l_4 \sin(\gamma) + \sqrt{h^2 + l_4^2 \sin^2(\gamma) - (k - x_C)^2}}{k - x_C - h} \right) \tag{3.2}$$

where $k = w + l_1$ and $h = l_2 - l_4 \cos(\gamma)$.

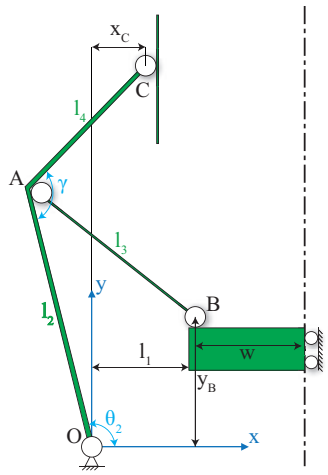

Figure 3.6 Finger kinematics. The rigid-body topological model illustrates the main geometric parameters and variables.

By appropriately bounding x_C, constraints on θ_2 and y_B are derived, enabling the determination of the platform displacement required for finger actuation.

3.2.3 Design for Additive Manufacturing

The PLG was designed for fabrication via Additive Manufacturing (AM), specifically using the Material Extrusion (MEX) process. This process involves depositing softened material layer-by-layer on a moving surface. The chosen AM approach influences design decisions, such as joint thickness, which is limited by the printer's resolution. Linear guides are also designed to avoid the need for supports.

The prototype was fabricated using a *MarkTwo* printer by *Markforged*, employing *Onyx*, a *Nylon-12* composite reinforced with short carbon fibres. This material offers excellent mechanical properties and high elongation at break (25%), making it ideal for compliant mechanisms. The total build time was approximately six hours, with an estimated cost of €6.18.

3.2.4 Linear Guides, Positive Drive Cam, and Spring

The vertical motion of the platform, as shown in Fig. 3.4, is achieved using a linear guide mechanism. Specifically, the platform features an extension that slides relative to the chassis, where this extension is joined to a slider. The special geometry of the linear guides ensures stable movement. Joints are designed to maintain minimal gaps—0.2 [mm] in this case—ensuring smooth motion without compromising stability.

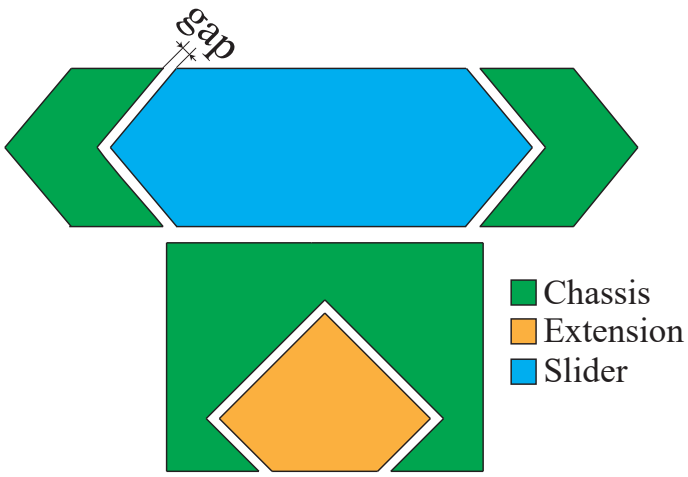

Figure 3.7 Cross-sections of the linear guides.

To enable fabrication without additional supports, the unsupported sections of the linear guides are oriented at 45° relative to the build platform. Fig. 3.7 illustrates the cross-sectional geometry of the linear guides.

Positive Drive Cam Mechanism. A positive drive cam mechanism, integrated into the slider, controls the position of the gripper fingers. The cam follower is realized with a metal pin installed post-manufacturing. As the pin follows its path, it reaches four key positions, illustrated in Fig. 3.8 and described below:

- In the starting configuration (①), the fingers remain open, with the pin at its highest position.
- When the gripper pushes against the object, the moving platform rises, transitioning the pin to its lowest position on the right (②).
- Once the load is released, the pin settles into the stable, closed-finger position (③).
- Further movement of the platform releases the fingers, moving the pin to its lowest left position (④).

Elasticity within the mechanism ensures the pin automatically returns to the starting position, reopening the fingers completely.

Pre-loaded Spring. A spring, connecting the slider to the chassis, supports the pin's movement through the cam path. The spring, designed with a repeated S-shape, is shorter

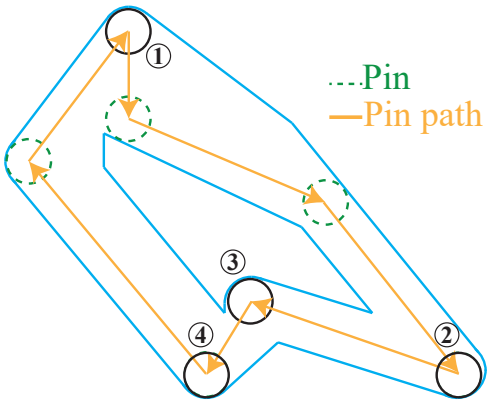

Figure 3.8 Positive drive cam. The diagram illustrates the cam path and pin motion through the four key positions (① to ④).

than the required distance at the end of the printing process. After fabrication, the spring is extended to connect with the slider, introducing a slight pre-load that enhances the system's operation. This configuration is also visible in Fig. 3.4.

3.3 PLG Virtual Prototype

To verify the design before physical testing, virtual simulations were conducted using the Finite Element Method (FEM) and the Pseudo-Rigid Body (PRB) approximation. Simulations were performed using the *Recurdyn* MultiBody Computer-Aided Engineering (CAE) software.

FEM simulations require substantial computational resources due to the dense mesh needed and the inclusion of three contact pairs: two at the fingertips and one between the cam pin and its guide. To simplify the virtual model and reduce computational time, a PRB approximation was employed, replacing flexible components with rigid bodies connected by spring-loaded joints. The optimization process for the PRB model involved matching the stiffness and pivot locations to replicate the FEM results, as detailed in Bilancia et al. (2019).

Material simulations were conducted with an elastic modulus of 1.4 [GPa], which, while lower than the manufacturer's datasheet value, aligns with experimental findings in the literature Bárnik et al. (2019); Vanaei et al. (2022).

3.3.1 Spring and Cam Flexure PRB Models

The pre-loaded spring was modeled in *Recurdyn* as a spring element with parameters derived from FEM simulations, including the pre-load force $F_{pre-load}$ and stiffness coefficient $K_{spring} = \frac{F_{max} - F_{pre-load}}{\Delta x}$, as shown in Fig. 3.9.

Similarly, the positive drive cam flexure was modeled with an equivalent stiffness coefficient K_{cam}. The stiffness value was optimized using the *Recurdyn* optimizer to ensure the PRB model accurately replicates the cam's behavior under deformation. This process involved applying a torsional moment M to the cam flexure and minimizing the error between the FEM and PRB displacement trajectories.

The optimization required 52 simulations, with a total computation time of 18[s] on a workstation equipped with an Intel Xeon E3-1270 v5 @ 3.6 GHz and 32 GB RAM, achieving a trajectory error of less than 1%. Fig. 3.10 shows the comparison between FEM and PRB trajectories.

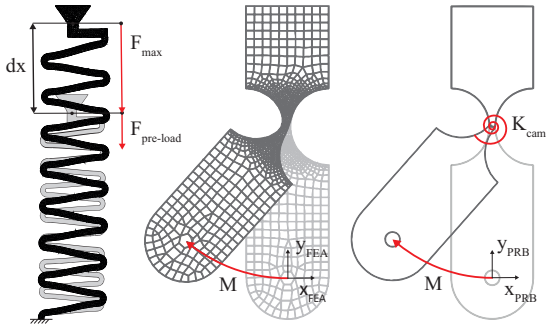

Figure 3.9 PRB model of the compliant spring (left) and positive drive cam (right).

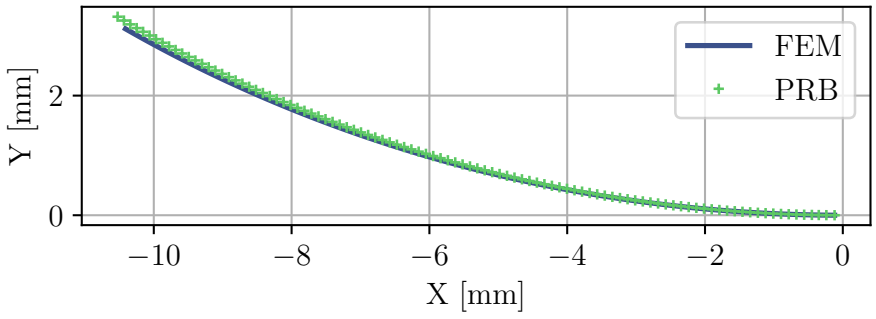

Figure 3.10 Comparison of displacement trajectories between FEM and PRB models for the cam.

3.3.2 Fingers PRB Model

Unlike the cam, which was approximated using a single torsion spring, the gripper fingers required a more complex PRB model with multiple springs. Each small flexural pivot and the thickest beam (l_4) were modeled with single torsion springs, while the slender beam (l_3) was represented by four torsion springs to capture its greater deformation Venkiteswaran and Su (2015).

The optimization objective was to match the contact force F_c exerted by the flexible finger against a square object (21 [mm] x 21 [mm]) during the initial grasping phase (① to ② in Fig. 3.8). This required 153 simulations, totaling 1120[s]. The PRB model's runtime of 7[s] compares favorably to the 12600[s] required for FEM, achieving a force error below 3.5%.

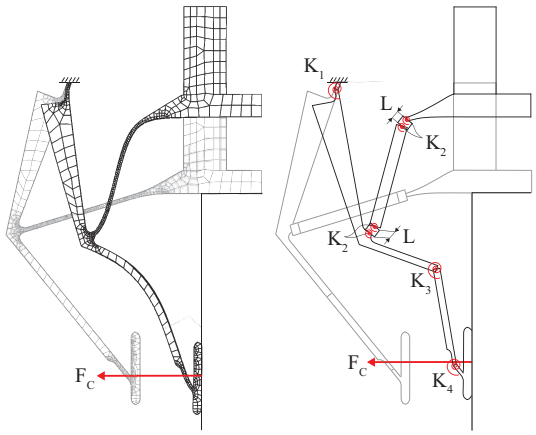

Figure 3.11 3D view and PRB model of the gripper finger.

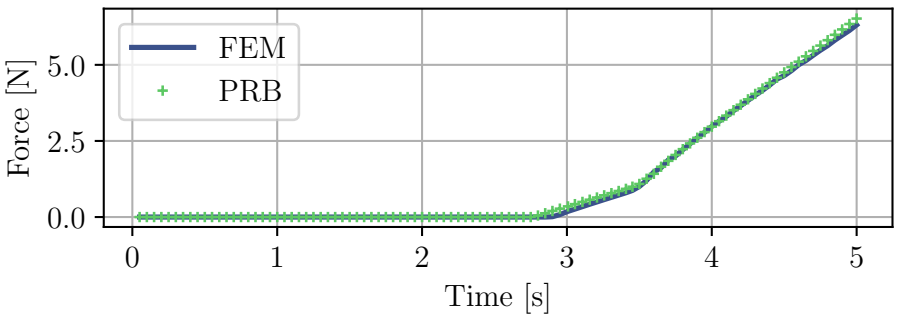

Figure 3.12 Contact force comparison between FEM and PRB models for the finger.

The optimized PRB model parameters, including pivot stiffnesses and positions, are summarized in Table 3.1.

Table 3.1 Optimized parameters for the PRB model.

Subsystem	Variable	Value
Spring	K_{spring}	1.936 [N/mm]
	$F_{preload}$	4.22 [N]
Cam flexure	K_{cam}	120.745 [Nmm/rad]
Finger	L	1.403 [mm]
	K_1	196.043 [Nmm/rad]
	K_2	163.869 [Nmm/rad]
	K_3	65.933 [Nmm/rad]
	K_4	70.623 [Nmm/rad]

3.3.3 PRB Model of the Gripper

Following the optimization of the individual components, the final step involved simulating the entire gripper mechanism. By employing the PRB model, the simulation of the complete gripping/releasing process was performed in substantially less time compared to the flexible model, which required over 27,000 s for the gripping phase alone, while the PRB simulation required approximately 180 s. The simulation was designed to replicate the actual behavior of the gripper and the same conditions used in subsequent experimental tests (detailed in the next section). Thus, it accounted not only for the contacts between the fingertips and the gripped component but also for the contact between the gripped component and the linear guide.

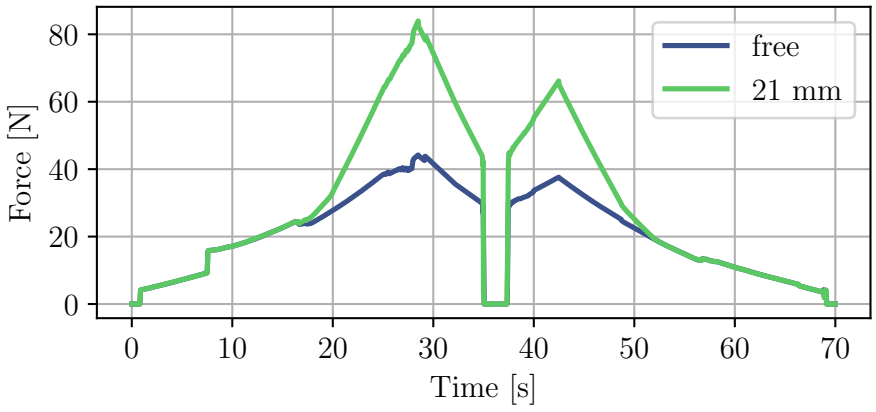

Figure 3.13 PRB model: force simulation with and without a gripped object.

This simulation confirmed the correct operation of the positive-drive cam mechanism and provided a preliminary estimation of the forces acting on the gripper. Fig. 3.13 illustrates the forces required to activate the mechanism both with and without the gripped object (83 N and 44 N, respectively). Additionally, Fig. 3.14 presents the measured gripping force of

the device, which is approximately 5 N when the positive-drive cam is in its lowest stable configuration (i.e., position ③).

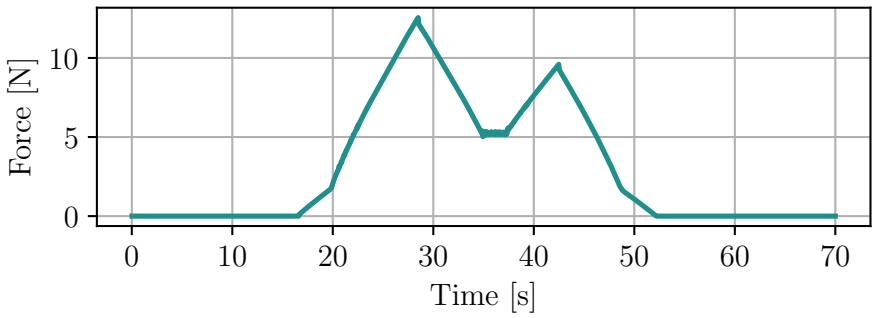

Figure 3.14 PRB model: gripping force with a 21 mm x 21 mm square cross-section object.

3.4 Mechanical Characterisation

3.4.1 Test Campaign

As introduced earlier, the gripper was designed to handle objects with two parallel flat faces. The following tests were conducted to quantitatively evaluate the gripper's performance:

1. **Locking/unlocking test without a workpiece**. The gripper was operated without a workpiece while measuring the force and displacement required to open and close the fingers. This test quantified the forces needed to activate the push-latch mechanism.

2. **Locking/unlocking test with workpieces**. The gripper was operated with workpieces of various sizes while measuring the force and displacement required to open and close the fingers. This test quantified the additional forces required to grasp the workpieces.

3. **Force closure pull-out test**. The force required to pull the object out of the gripper when friction alone holds the workpiece was measured for various object dimensions. This test quantified the maximum load the gripper could bear in force closure mode.

4. **Form closure pull-out test**. The force required to remove the object when geometric coupling holds it was measured. This test quantified the maximum load the gripper could sustain in form closure mode.

The locking/unlocking tests (both with and without workpieces) were conducted using a *Zwick Roell Z050* testing machine equipped with a 50 kN load cell, rated Class 1 according to the ISO 7500-1 standard. The test objects were anchored to the machine's base using custom fixtures, while the gripper was mounted on the moving traverse using dedicated supports. The experimental setup is illustrated in Fig. 3.15.

The tests were performed by imposing a predefined motion of the moving traverse at a constant speed of 30 mm/s, while recording the forces using the load cell. The displacement profile is presented in Fig. 3.16 (top graph).

The pull-out tests were conducted with a *PCE-DFG N 500* dynamometer by PCE Instruments, which has a full-scale load of 500 N and a resolution of 0.1 N. The workpieces used for the tests were parallelepipeds with a square cross-section (height: 60 mm) and side lengths varying from 21 mm to 39 mm in increments of 3 mm.

Figure 3.15 Experimental setup. The figure depicts the configuration used for the locking/unlocking tests.

3.4.2 Results

Fig. 3.16 presents the results of the locking/unlocking test without a gripped object. The force profile shows two peaks: the first corresponds to the stable closure of the fingers, while the second corresponds to the unlocking phase where the mechanism opens. In the locked position, the load measured by the testing machine drops to nearly zero, consistent with the design, which does not require power to maintain the grasp. The force needed to activate

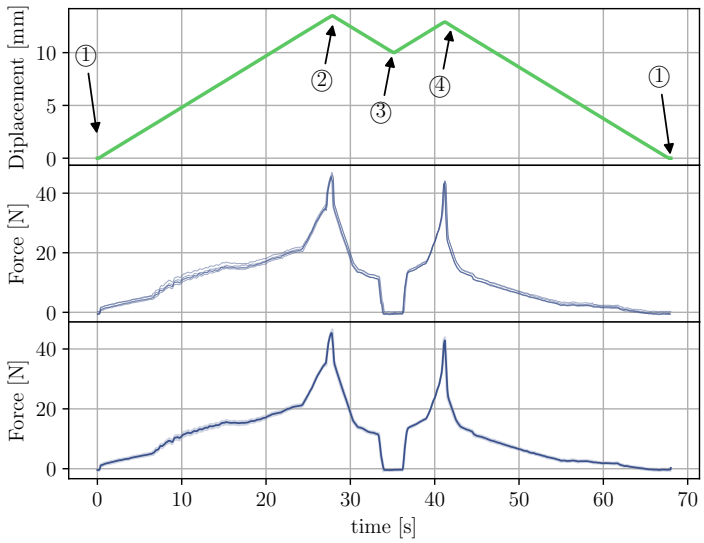

Figure 3.16 Loading test without a workpiece. The top graph shows the displacement commanded to the moving traverse as a function of time. The middle graph represents the forces measured by the load cell in five test repetitions as a function of time. The bottom graph represents the average of the force profile as a function of time and its standard deviation (represented as a shaded area -barely visible).

the mechanism was approximately 45 N. The force-displacement cycle is also illustrated in Fig. 3.17.

Fig. 3.18 shows the results for tests with varying workpiece sizes. As expected, the force required to operate the gripper increases with the size of the workpiece, ranging from 76 N to 83 N for the first peak and 76 N to 96 N for the second.

The pull-out tests results, presented in Fig. 3.19, demonstrate that the gripper can hold objects approximately eight times heavier in form closure mode compared to force closure mode. In both modes, the pull-out force increases with the workpiece size due to the larger contact area and greater deformation of the gripper's fingers.

Lastly, Fig. 3.20 compares the force profiles from simulations and experimental data, showing good agreement despite minor discrepancies attributed to PRB model simplifications and material behavior variations. The PRB model proves to be a valuable tool for assessing gripper performance before prototyping.

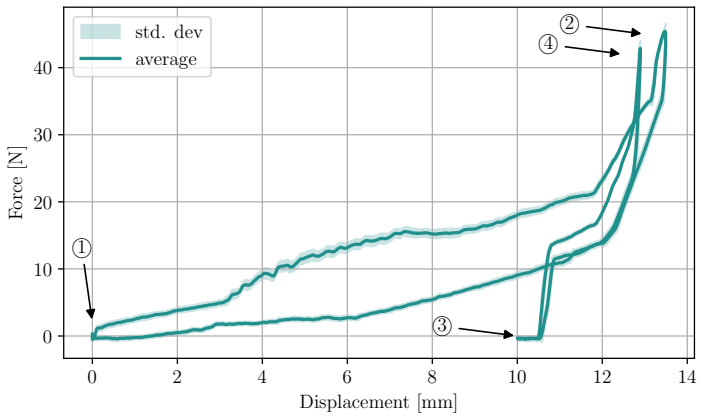

Figure 3.17 Loading test without a workpiece. The graph illustrates the average force-displacement profile along with its standard deviation.

Figure 3.18 shows the results of the locking/unlocking test with varying object sizes. This test was repeated ten times for seven different object widths. The graph clearly depicts the expected two-peak behavior observed in the test conducted without a workpiece, where the force drops to zero at the rest condition (i.e., position ③). Additionally, the figure highlights that the force required to operate the gripper increases with the object size, rising from 76[N] to 83[N] for the first peak and from 76[N] to 96[N] for the second peak. This increase is consistent with the fact that larger objects induce greater deformation in the fingers, thereby requiring more force to deform them.

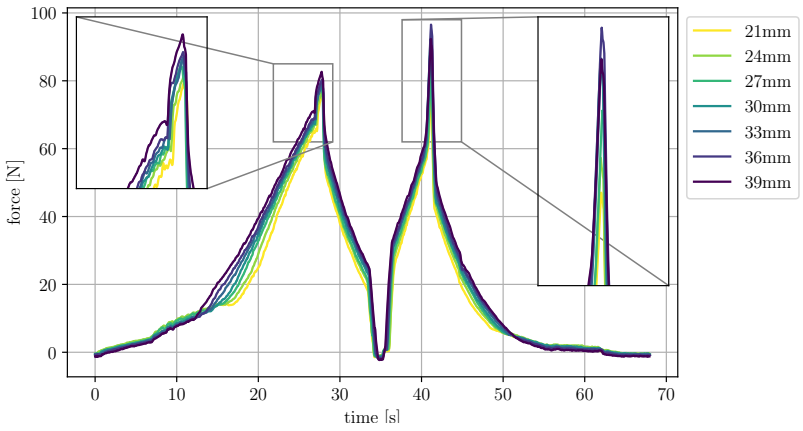

Figure 3.18 Loading tests with varying workpiece sizes. The graph presents the force profiles during grasping tests for different object sizes. The test was repeated ten times for each of the seven object widths. The curves in the graph represent the average for each of the seven test conditions.

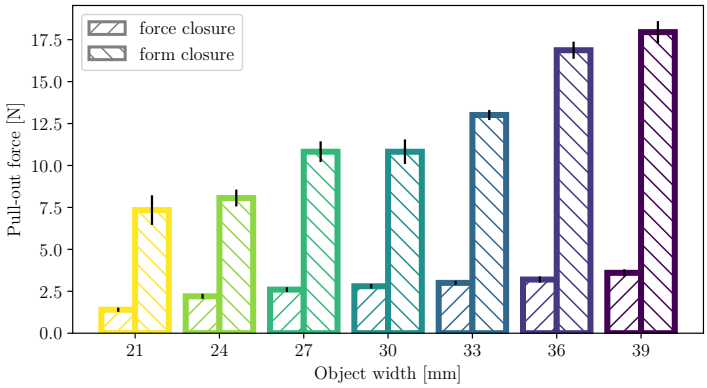

Figure 3.19 Pull-out test. The graph compares the pull-out forces measured during tests for both the force closure and form closure operation modes. The test was repeated ten times for each of the seven object sizes. The bar values represent the average pull-out force for each object width, with standard deviations indicated by black error bars superimposed on each test condition.

Figure 3.19 illustrates the results from the pull-out tests for both force and form closure operation modes. These tests were repeated ten times for each condition, with the measured values averaged and plotted. The graph shows that the form closure mode enables grasping objects approximately eight times heavier than in the force closure mode. Furthermore, as the object sizes increase in both cases, so does the force required to pull the object out of the gripper. This increase in force is due to the greater finger deformation required as the object size grows. Larger objects thus correspond to: *i)* increased contact forces in the force closure mode; *ii)* higher forces necessary to deform the fingers until the object is released. Additionally, Figure 3.20 evaluates the fidelity of the simulations by comparing the measured and simulated force profiles. The upper plot represents the force profile when activating the mechanism without an object (free condition), while the lower plot shows the condition when grasping a 21[mm] wide object. In these simulations, a friction coefficient of $\mu = 0.3$ was included, determined through a trial-and-error process to match experimental tests. While there is a slight mismatch in the force values, particularly in the free mechanism activation condition, this can be attributed to factors such as the simplifications made in the PRB model. Additionally, friction forces within the mechanism were neglected for computational simplicity, and slight variations in the Young's modulus of the AM material (i.e., *Onyx*) after loading/unloading may contribute to this mismatch. Despite these discrepancies, the PRB model captures the main characteristics and overall behavior of the mechanism, accurately predicting peak forces and proving to be an effective design tool for assessing gripper

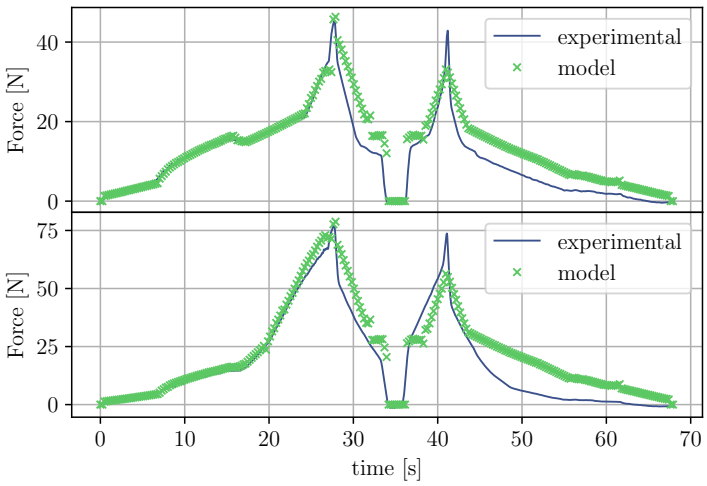

Figure 3.20 Force profile comparison. The figure compares the force profiles measured experimentally and those derived from the model for the activation of the push-latch mechanism. The upper plot represents the force profile for the free condition (i.e., no object present), while the lower plot shows the force profile when grasping an object of 21 mm width.

performance before physical prototyping. Finally, to compare the presented design with state-of-the-art industrial grippers, the PLG C-factor (measured in [J/Kg]) is computed and shown in Figure 3.21. As defined in Birglen and Schlicht (2018), the C-factor of a gripper is calculated as the ratio of the force it generates to its weight, multiplied by the stroke. As seen in the plot, the proposed PLG gripper (due to its low weight and lack of actuators) outperforms most existing commercial solutions. Furthermore, the proposed solution can be manufactured at ultra-low cost, making it attractive for industrial applications where plug-and-produce, easily replaceable devices are required.

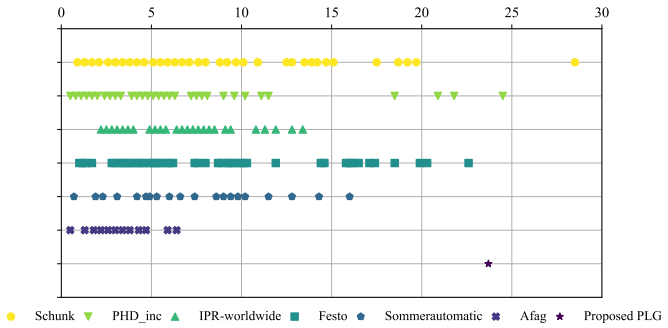

Figure 3.21 Comparison of C-factor values commonly used in the industry and those proposed in this work, adapted from Birglen and Schlicht (2018).

3.5 Limitations and future work

The experiments presented in this chapter demonstrate that Material Extrusion (MEX) of Onyx components is a viable method for creating a monolithic robotic gripper for pick-and-place tasks. Additionally, the results offer insights into potential areas for further enhancement.

Initially, it is important to note that the tests conducted in this research were limited to a few dozen cycles. The findings highlight the need for further investigation into the fatigue performance of the PLG, especially considering the repetitive nature of industrial gripper operations and the fact that their operational lifetime often exceeds 10^6 cycles. However, literature on the fatigue behavior of additively manufactured thermoplastics remains limited, and more studies are needed.

Another area with room for improvement is the ratio between the required activation force and the resulting grasping force. Even under the most favorable form closure operation mode, this ratio is approximately 5.4, indicating that to lift an object of a given weight, the gripper must exert a force 5.4 times greater than the weight of the object. This suggests that the push-latch design may not be optimal for handling delicate objects.

Despite the aforementioned limitations, this work demonstrates that MEX of Onyx components holds significant promise for creating effective monolithic robotic grippers for pick-and-place applications. Furthermore, the experimental results reveal good repeatability of the end-effector's performance, which can be attributed to the use of compliant joints.

Moreover, the simulation method based on the PRB approximation proves to be a robust, precise, and efficient tool for optimizing the design and adapting it to objects of varying sizes and shapes.

Chapter 4

Delta-Flex: a monolithic delta robot

4.1 Contribution

The current chapter presents the development and validation of a compliant Delta robot with a monolithic structure, which has been fabricated using additive manufacturing (AM). As seen in 1.2.1, additive manufacturing provides designers with the ability to create mechanisms that require no assembly Lussenburg et al. (2021b), commonly referred to as monolithic mechanisms. These systems stand out because they are ready for use immediately after the manufacturing process is complete. The use of monolithic mechanisms offers multiple advantages, including reductions in both time and cost by eliminating the need for assembly operations, less tight tolerance requirements, functional integration, and the absence of additional components such as bearings or fasteners which contributes to overall weight reduction. These benefits make monolithic mechanisms an interesting solution for applications where time and cost efficiency are paramount.

This study draws inspiration from the works of Bruyas et al. (2014), Rommers et al. (2021), and Naves et al. (2021). The work of Bruyas et al. (2014) is significant for being one of the earliest to present a 2DOF mechanism fabricated monolithically using multi-material printers. In 2021, Rommers et al. (2021) introduced the “Tetra1 ” and “Tetra 2” designs for large range of motion spherical joints, with the latter being particularly well-suited for additive manufacturing and used as one of the key building blocks of the current work. Additionally, Naves et al. (2021) demonstrated the feasibility of high-precision parallel robots with large workspaces, utilising only compliant joints. Some of the key concepts from these works were adapted and integrated into the present work.

The contributions of this design lie in four main differences between the presented mechanism and existing Delta robot implementations in the literature:

1. previous implementations mainly focused on flexure hinges, whereas the current design heavily relies on the “Tetra 2” spherical joint to achieve higher mobility;
2. the presented mechanism is larger, resulting in a larger workspace, which in turn complicates manufacturing and the achievement of high precision;
3. all other compliant delta implementations (with the notable exception of Correa et al. (2016)) only focused on the final articulated quadrilaterals, whereas a full robot was developed in this work;
4. it is completely monolithic and is fabricated in a single manufacturing step.

4.2 System Design and Implementation

Compliant joints often face limitations in their range of motion, presenting a significant obstacle to achieving large workspaces for robotic systems. However, parallel architectures are particularly advantageous for designs incorporating flexible joints, as evidenced by the work of Naves et al. (2021), since the required motion range for individual joints is typically smaller than in serial architectures. Considering these factors, the Delta architecture was chosen for this study. The system implementation is depicted in Fig. 4.1, which provides a comprehensive view of the DeltaFlex and its main components.

Despite the benefits of the parallel architecture, achieving a wide range of motion for the joints posed challenges. To overcome this limitation, a two-stage cart-wheel flex-pivot was employed for the rotational joint of each arm at the base. Similarly, the four spherical joints of each arm were designed based on the “Tetra 2” joint introduced by Rommers et al. (2021), with slight modifications to extend the range of motion and prevent self-collision (refer to Kargar et al. (2024) for further details). A comparison between the original joint design by Rommers et al. and the spherical joint used in the DeltaFlex is presented in Fig. 4.2.

A Design for Additive Manufacturing (DfAM) approach was employed throughout the development of the robot. Powder bed fusion was selected as the primary manufacturing method due to its cost efficiency and its ability to fabricate parts without requiring support structures. Nevertheless, the geometries produced through the DfAM process are also well-suited for fused material extrusion printers, which are more widely available.

To make the design compatible with material extrusion, the structure had to be divided into three separate parts, as shown in Fig. 4.3. While this adaptation alters the monolithic nature of the mechanism, it does not deviate significantly from the fundamental design philosophy, as the resulting mating interfaces do not demand tight coupling tolerances.

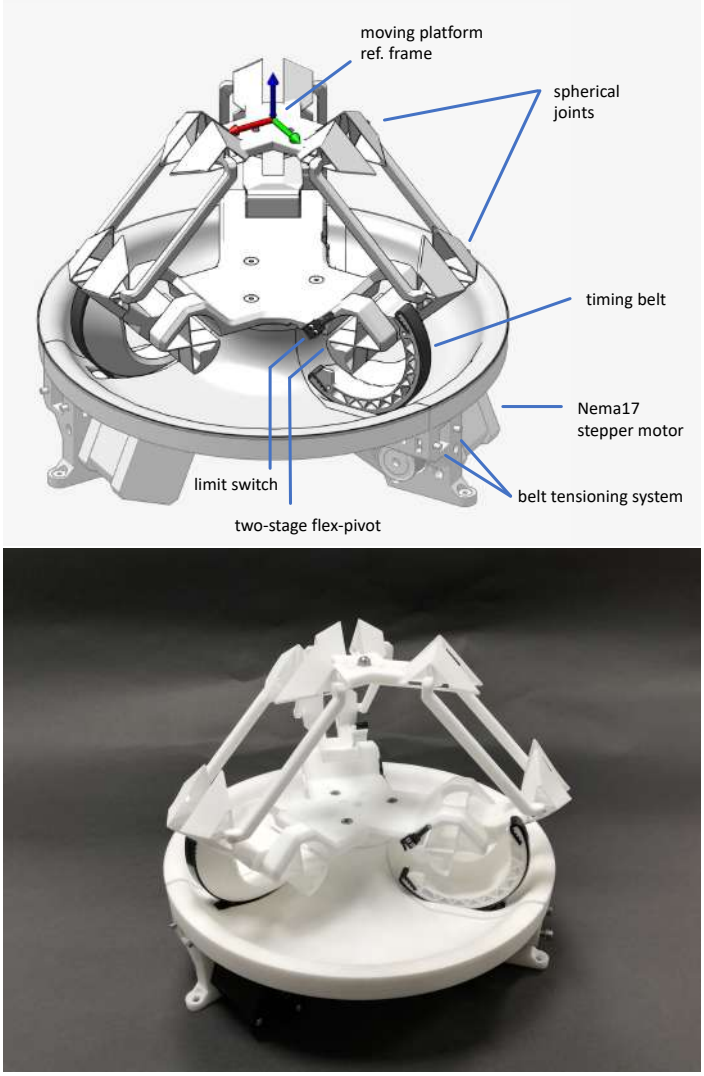

Figure 4.1 CAD view and photograph of the DeltaFlex

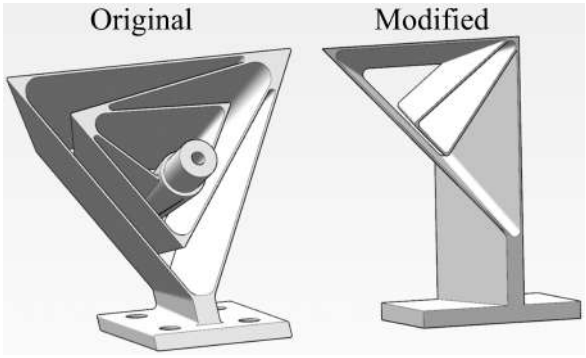

Figure 4.2 Comparison between the spherical joint adopted in this work and the original design by Rommers et al. (2021)

All flexures within each arm were oriented to develop orthogonally to a common direction, ensuring that selecting this orientation as the build direction would maximize their mechanical strength. The “Tetra 2” spherical joints were designed with a 45° inclination, eliminating the need for support structures and avoiding surface quality degradation in critical regions. Furthermore, horizontal geometric features were extended at an angle greater than 45° to render them self-supporting, and overhangs were minimized wherever possible. The build strategy for the modified part, adapted for material extrusion additive manufacturing, is illustrated in Fig. 4.4.

The mechanism described in this study was fabricated using powder bed fusion on a 3D Systems ProX SLS 6100 machine with DuraForm PA as the construction material. DuraForm PA is a robust polyamide 12 thermoplastic (Nylon) with excellent structural properties and near-isotropic behavior after manufacturing. Its high deformation-at-break value (14%) makes it particularly well-suited for compliant mechanisms. Flexures were designed with a thickness of 0.7 mm, which was determined to be the minimum reliable thickness manufacturable on the ProX SLS 6100.

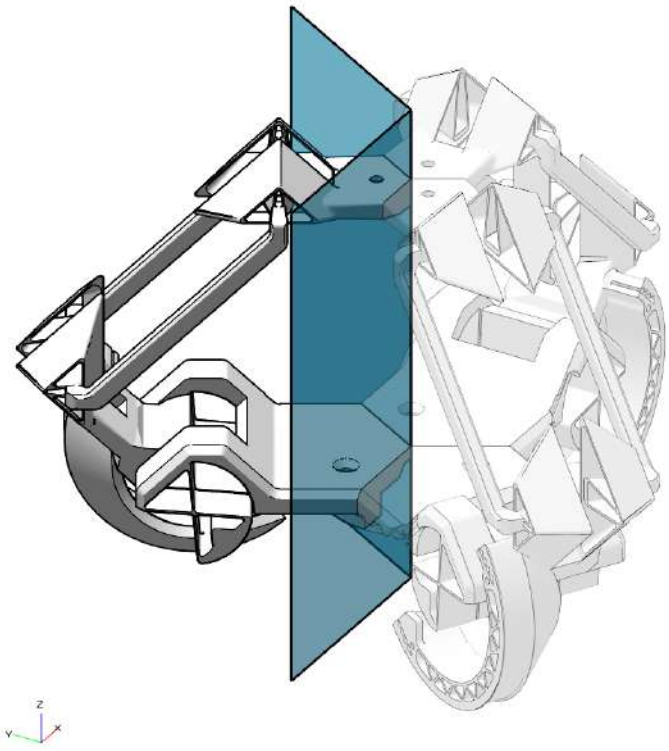

Figure 4.3 Sub-division of the mechanism for compatibility with material extrusion additive manufacturing.

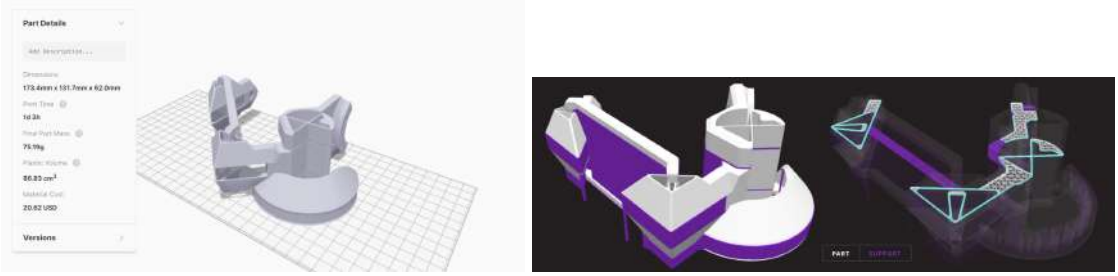

Figure 4.4 Build strategy. The figure shows the overall view of the divided part (top) and a sliced view (bottom) in the Markforged Eiger slicing software. Notably, the bottom-right detailed layer view demonstrates that the flexures are support-free, which is a key aspect of the design.

Each arm was actuated using Nema17 stepper motors, chosen for their high holding torque and ease of control. The motors used had a step angle of 1.8°, a holding torque of 0.59 Nm, and an input voltage of 2.80 V. The driving motors were connected to driven pulleys integrated directly onto the first link of each arm via timing belts, achieving a transmission ratio of 3.8:1. The belt tensioning mechanism, shown in detail in Fig. 4.5, was integrated directly into the support structure of the device.

Motor control was handled by an Arduino UNO WIFI rev.2 (ATmega4809 8-bit microcontroller) with a 3-Axis CNC/Stepper Motor Shield and A4988 stepper drivers. Limit switches (Omron D2MQ-4L-105-1) were installed on each axis to enable the device's initial homing.

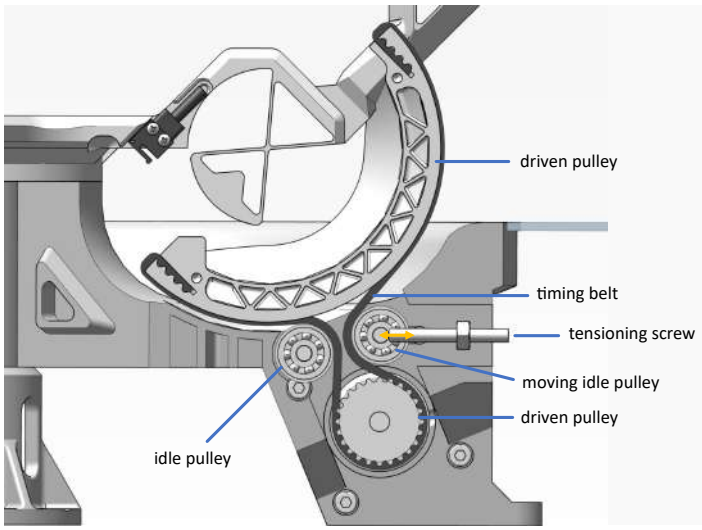

Figure 4.5 Belt tensioning mechanism.

To promote reproducibility, all models and resources have been made publicly available in a GitHub repository[1].

4.3 Experiments

The quantitative analysis of DeltaFlex's performance concentrated on two main parameters: rigidity and accuracy. The evaluation of rigidity involved measuring the device's capacity to withstand applied forces, an essential aspect for ensuring movement accuracy under various operational conditions. While traditional robots with rigid links and bearings typically do not experience this issue, it becomes more critical in robots that feature flexible joints. The rigidity assessment was conducted through two separate experiments.

The first experiment measured the mechanism's translational rigidity under typical operating circumstances, where the mobile platform moved parallel to the stationary base. The second experiment aimed to assess the mechanism's resistance to lateral forces that could cause the mobile platform to tilt, which could hinder the system's ability to move exclusively along the x, y, and z axes without unintended rotational motion.

Lastly, a third experiment focused on quantifying the mechanism's accuracy by evaluating its repeatability.

4.3.1 Translation Stiffness Test

The stiffness of the device was characterized using a *Zwick-Roell Z050* tensile/compression testing machine, fitted with a load cell rated for a 50[kN] full-scale load (with Class 1 accuracy according to the ISO 7500-1 standard). During the testing process, the robot's base was fixed, while the end-effector was securely attached to the moving traverse. The traverse was moved, applying a load to the robot, which then deformed, with forces and displacements being recorded throughout the process. The speed of the moving traverse was set to 30 mm/min. Two distinct configurations were examined: in the first, the robot was installed with the moving platform perpendicular to the direction of motion of the moving traverse, while in the second configuration, the moving platform was aligned parallel to the direction of motion of the moving traverse. Fig. 4.6 shows these configurations. Starting from the home configuration, both loading conditions were applied bidirectionally by performing both descending and ascending movements of the moving traverse. This procedure enabled

[1] https://github.com/made-iit/public/deltaflex

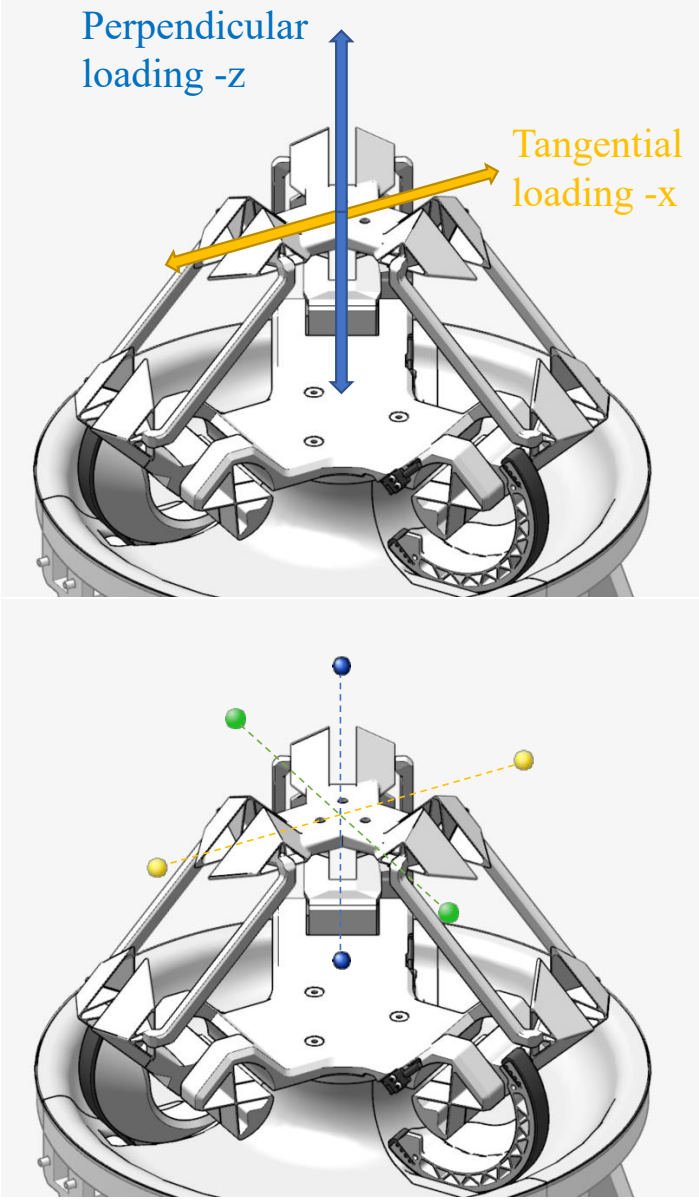

Figure 4.6 Different load configurations and reference configurations. The figure represents the perpendicular and tangential loading directions (left), as well as the end-effector positions corresponding to the six test configurations. The colour coding (x in yellow, y in green and z in blue) is the same used in Fig.4.11.

the evaluation of the robot's behavior in opposing directions. To ensure statistical reliability, the test was repeated five times under all conditions, and the results were averaged.

4.3.2 Offset Loading Test

The second evaluation of stiffness was carried out as follows. The end effector was repositioned into six reference configurations, each placed near the boundaries of the robot's workspace. The input joints were then secured using a custom fixture to eliminate the influence of the belt transmission on the experimental results. The Cartesian coordinates of the six reference configurations are listed in table 4.1. Once the input joints were locked, the position and orientation of the end effector were measured. Calibrated weights of 50[g], 100[g], 150[g], and 200[g] were then applied to the moving platform at an offset position 200[mm] from the end effector's center. This configuration is equivalent to applying a wrench with components $[0, 0, -9.81 \cdot W, 0, 0.2 \cdot 9.81 \cdot W, 0]$ to the end effector (i.e., a negative force in the z direction and a positive torque in the y direction), where W denotes the weight of the applied calibrated load. For reference, the maximum applied force was -1.96[N] and the maximum applied torque was 0.39[Nm]. For each loading condition, the end effector's position and orientation were measured three times. Measurements were conducted using a Shining 3D Einscan XH 3D scanner. The laser modality was employed in combination with marker-based tracking to enhance measurement accuracy. Under these conditions, the scanner had an accuracy of 0.04[mm]. After measuring all positions and orientations, the Euler angles representing the three-dimensional rotations of the end effector were extracted. This was accomplished by fitting coordinate system features to the obtained scans. It should be noted that this fitting procedure can result in errors on the order of 0.5°. The configuration of the moving platform was measured both before and after the application of the loads. This approach allowed the differentiation between the platform's tilting due to displacement from the home configuration and the tilting caused by the applied loads. This method was essential as it would not have been possible to perform using a material testing machine.

Table 4.1 Cartesian coordinates (in millimetres) of the six reference configurations used for the tests

x+	[38, 0, 0]
x-	[-38, 0, 0]
y+	[0, 38, 0]
y-	[0, -38, 0]
z+	[0, 0, 42]
z-	[0, 0, -42]

4.3.3 Repeatability Test

The third test was conducted to evaluate the repeatability of the robot's performance. This parameter is vital for tasks that require high precision and consistency (e.g., in manufacturing processes). For this purpose, the robot's end-effector was moved to six different reference configurations near the boundaries of the robot's workspace, with twenty repetitions for each configuration. In each repetition, the final position of the end-effector was measured using a *TESA 01811001 SwissTast* micrometric dial gauge (range: 0.2[mm], resolution: 0.002[mm], measuring force: 0.15[N]). To ensure repeatability, the probe made contact with an 8[mm] diameter calibrated, hardened stainless-steel sphere. The experimental setup is illustrated in Fig.4.7.

4.4 Results

The results from the stiffness test are shown in Fig.4.8.(a) for the case of perpendicular loading of the end-effector, and in Fig.4.8.(b) for the case of transversal loading. In both figures, the ascending load path (where the robot is subject to tensile force) and the descending load path (where the robot is subject to compressive force) are represented in green and blue, respectively. The curves represent the average of all experimental runs, and the shaded bands above and below the curves indicate the standard deviation of the data. Arrows are superimposed on the plots to mark the segments corresponding to the increasing and decreasing load phases. A linear fit to the force-displacement curve for the perpendicular

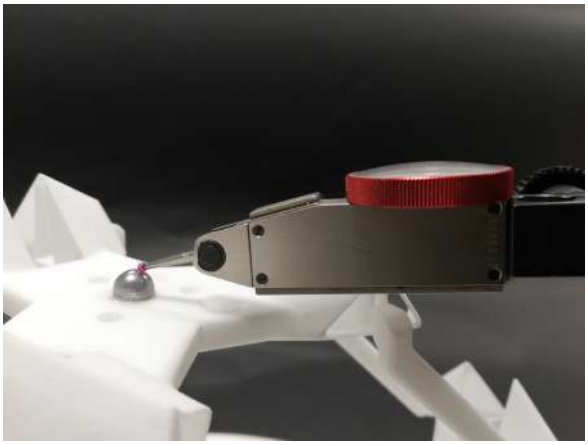

Figure 4.7 Repeatability test setup. The photograph shows the setup with the micrometric dial gauge and the calibrated steel sphere used in the tests.

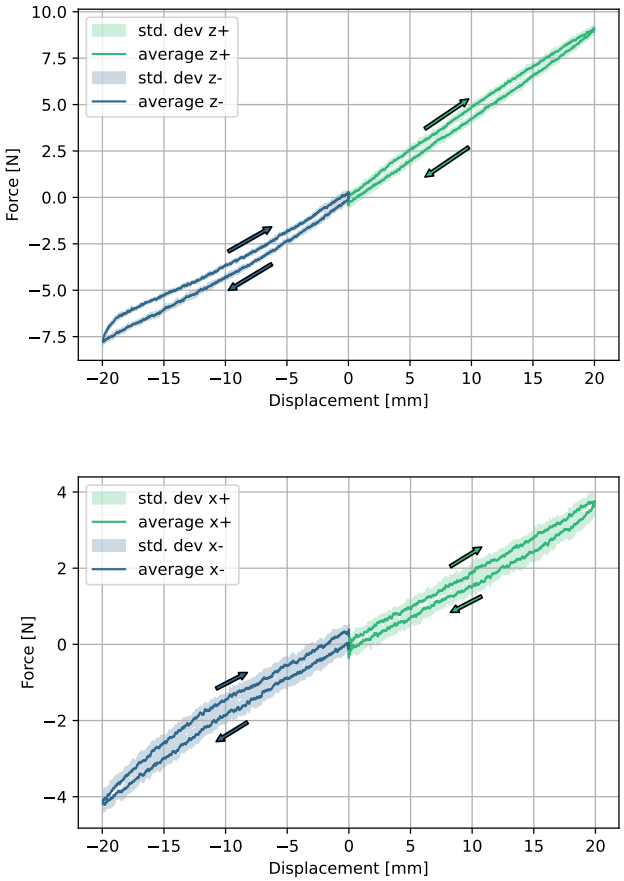

Figure 4.8 Experimental results of the stiffness tests. The figure shows the force-displacement curve for perpendicular loading (top) and for tangential loading (bottom).

loading case gives a stiffness value of 0.41[N/mm], while for the tangential loading case, the computed stiffness is 0.19[N/mm].

A key observation is that for each condition, the loading and unloading paths of the robot do not follow the exact same force-displacement trajectory, resulting in a narrow hysteresis loop. This is somewhat unexpected given the absence of bearings with moving parts and the fact that robot motion is solely due to the flexures' deflection, which should be almost frictionless. Further material testing was carried out to quantify the extent of hysteresis in the material. A detailed description of this additional test and its results can be found in Appendix A; the findings confirm significant hysteretic behavior within the material. Additionally, the force-displacement curve is not perfectly linear. This non-linearity may be attributed to either large deformations or non-linear material properties. Further experiments are required to determine the exact cause of this behavior. Despite these imperfections,

the overall stiffness of the robot is relatively low, indicating that the DeltaFlex achieves a wide range of motion while offering relatively low resistance to movement, (which is a desirable feature for compliant mechanisms). The results of the second stiffness evaluation are presented in Fig.4.9 and Fig.4.10, which provide several important insights. Figure 4.9 shows the translation errors of the platform in the six reference configurations when no external loads were applied. Although the error values were generally below 3[mm], some exceeded this threshold (consistent with previous studies, e.g., Mannam et al. (2021a,b)). As such, open-loop control would not be suitable for such a mechanism, and closed-loop position feedback would be necessary for accurate end-effector position control. This, however, presents the challenge of accurately measuring the end-effector's pose. Figure 4.10 illustrates the impact of offset loads on the end-effector's orientation. For configurations where the end effector underwent lateral translation in the y direction (i.e., the "y+" and "y-" conditions), a significant orientation drift between +8° and -12° was measured. The "x+" and "x-" conditions showed similar drifts, but in this case, the angles were confined between +7° and -8°. These findings suggest that the motion of the mechanism within its

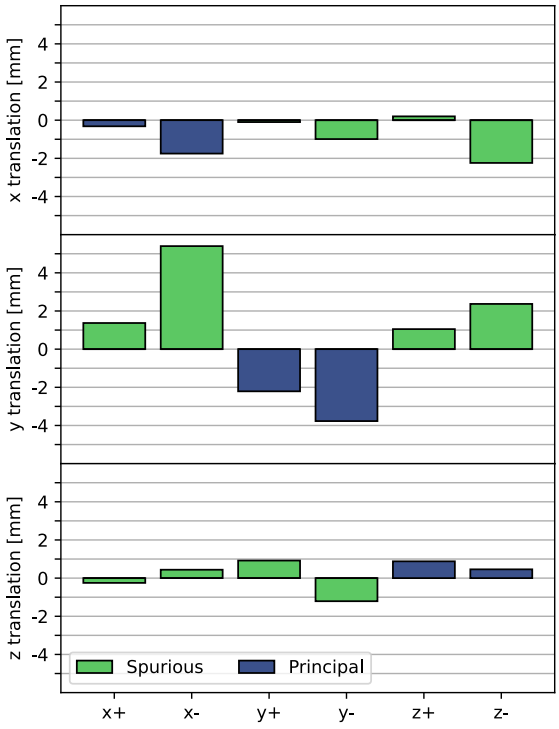

Figure 4.9 End effector translation errors. The figure shows the translation errors of the end-effector in the x, y, and z directions for the reference configurations. Errors in the primary directions are plotted in blue, while errors in non-primary directions are plotted in green. The corresponding test configurations are labeled as in table 4.1.

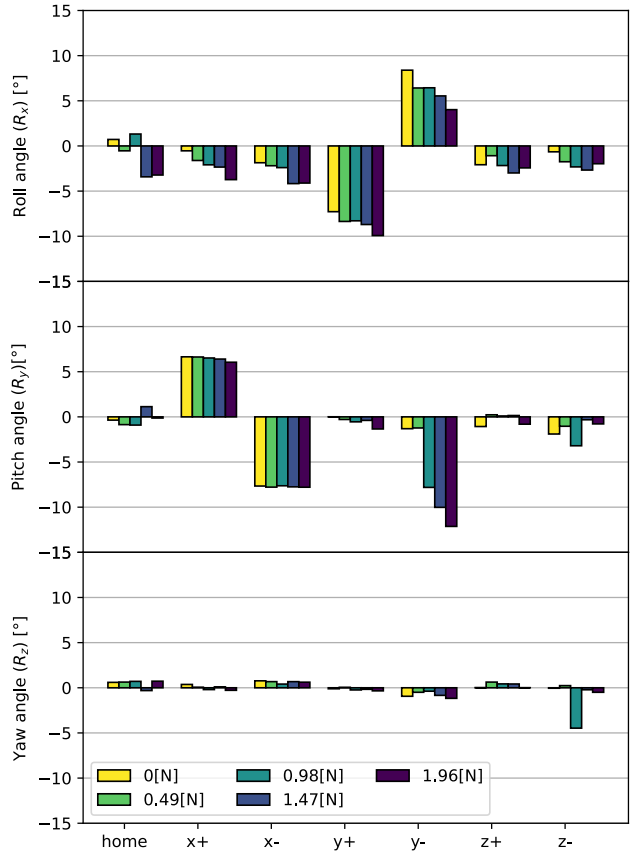

Figure 4.10 Results of stiffness tests under offset loads. The figure shows the roll, pitch, and yaw angles measured in seven reference configurations for five increasing offset loads. The corresponding test configurations are labeled as in table 4.1.

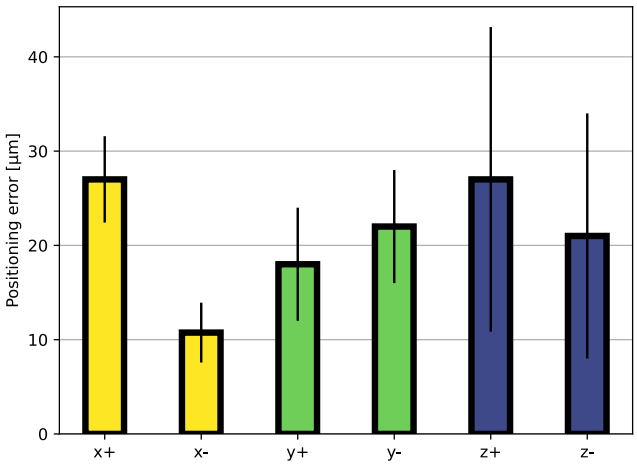

Figure 4.11 Repeatability test results. The histograms show the repeatability errors and their standard deviations for the six reference test configurations in table 4.1.

workspace influences the platform's tilting. Conversely, as expected, the displacement of the end-effector and the offset loads had a negligible effect on rotations around the z-axis (as seen in the z Euler angle graph). Figure 4.10 demonstrates that a linear increase in the applied offset loads leads to a proportional increase in the platform tilt across all configurations tested. This effect is particularly noticeable in the y Euler angle graph. Thus, the mechanism appears to exhibit linear behavior within the tested force range. Notably, the use of compliant joints resulted in larger orientation errors than would have been observed with a conventional design using traditional bearings. This aspect should be considered when evaluating the mechanism for future applications. Nevertheless, after a thorough evaluation of kinematic errors, the current design may prove useful for tasks requiring scanning or pointing motions. The results of the repeatability test are shown in Fig.4.11.

The plot illustrates that for the six selected test configurations, the average position shift is consistently below 30[μm], demonstrating the robot's excellent repeatability.

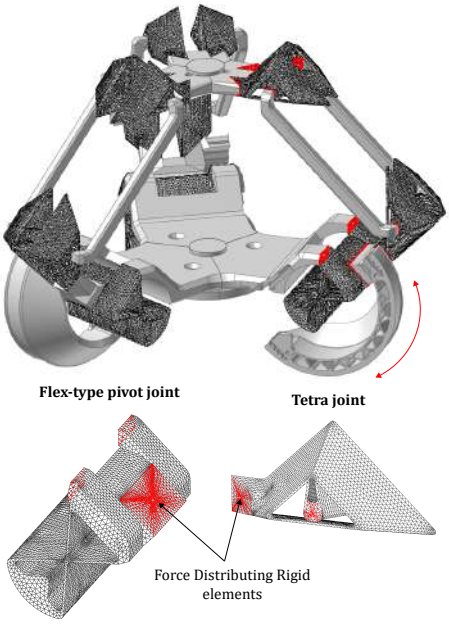

Figure 4.12 Hybrid model in RecurDyn. This figure displays the 3D model developed within the RecurDyn environment used for simulations. The meshed areas represent the flexible components, while the grey regions denote the rigid bodies.

4.5 DeltaFlex Virtual Prototyping

Simulating the structural and motion behavior of a robotic system is a powerful method for validating experimental outcomes. In this case, the DeltaFlex robot was simulated

using RecurDyn, a flexible multibody dynamics software, to corroborate the experimental findings related to stiffness analysis, direct kinematics, and Euler angles. This tool has been previously utilized by the authors for sizing and subsequent shape optimization of compliant joints and devices constructed using them Bilancia and Berselli (2021). By modeling the robot in a virtual environment, its behavior can be analyzed, and simulation results can be compared with experimental data, aiding in design decisions and geometry optimization of the compliant joints.

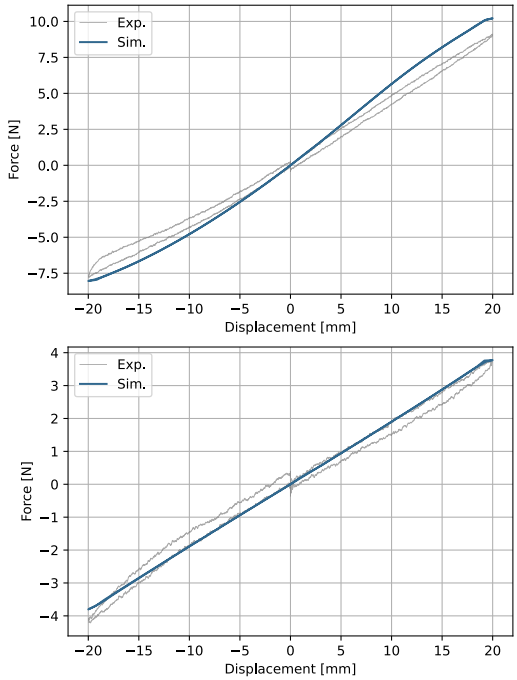

Figure 4.13 Stiffness simulation results in RecurDyn. The figure shows the force-displacement curve for both perpendicular loading (top) and tangential loading (bottom). The results from the RecurDyn simulations (denoted as "Sim.") are overlaid on the averaged experimental data (shown by the grey line, labeled "Exp.") to illustrate the correlation between the two sets of results.

For the simulation, the 3D model created in PTC Creo was imported into RecurDyn, as shown in Fig.4.12, and material properties for Nylon from RecurDyn's library were applied.

The links, base, and end-effector were treated as rigid bodies, while the flexures were meshed with a minimum and maximum element size of 0.2 and 1.2, respectively, and a triangular mesh type was used. To replicate the experimental conditions, a ±20[mm] displacement in both the horizontal and vertical directions was applied through a point on curve (PTCV) joint. The reaction forces at the joint were measured in response to the input displacement, allowing for the generation of force-displacement graphs for both loading

scenarios, as shown in Fig.4.13. The Young's modulus of the material was determined through experimental testing of material specimens according to ISO 527 standards (see Appendix A).

The results from the simulations corroborated the experimental data, indicating that the robot exhibits low stiffness in the desired directions of motion. For the vertical loading case, the force-displacement curve displayed a slight non-linearity, which can be attributed to the influence of large deformations. To further validate the experimental results regarding direct kinematics and Euler angles, an additional simulation was conducted. The same input rotations applied in the experiments were introduced into the FEA model in RecurDyn. The resulting output translations and Euler angles from the simulations were compared to the corresponding experimental measurements, as shown in Fig.4.14. The plots reveal a strong agreement between the simulation data and the experimental results. This suggests that, despite the approximations inherent in the simulation model, it accurately captures the overall behavior of the mechanism, including spurious roto-translations.

4.6 Assessment of Kinematic Errors

An additional benefit of the FEM hybrid model of the entire compliant mechanism is its ability to isolate and analyze the individual contributions of various joint errors to the overall kinematic error. In order to explore this, a subsequent analysis was performed to assess the effect of parasitic motion originating from the different flexures. Specifically, three distinct models were developed in the RecurDyn environment and compared. These models include:

- Model 1: *Fully Rigid Model*, where all joints are modeled as rigid bodies, represented by revolute and spherical joints.
- Model 2: A model where the three base cross-axis flexures are treated as rigid and substituted with revolute joints, while the spherical joints are modeled as flexible *Tetra 2* joints.
- Model 3: A model in which the compliant *Tetra 2* joints are replaced by rigid spherical joints, while the cross-axis flexures remain flexible.

To assess the accuracy of the models, the simulated motions were compared with a "baseline" model computed using analytical inverse kinematics. As a case study, a helical trajectory, involving motion in all three translational directions of the Delta robot's end-effector, was applied. For each configuration, the input joint rotations (i.e., the rotations of

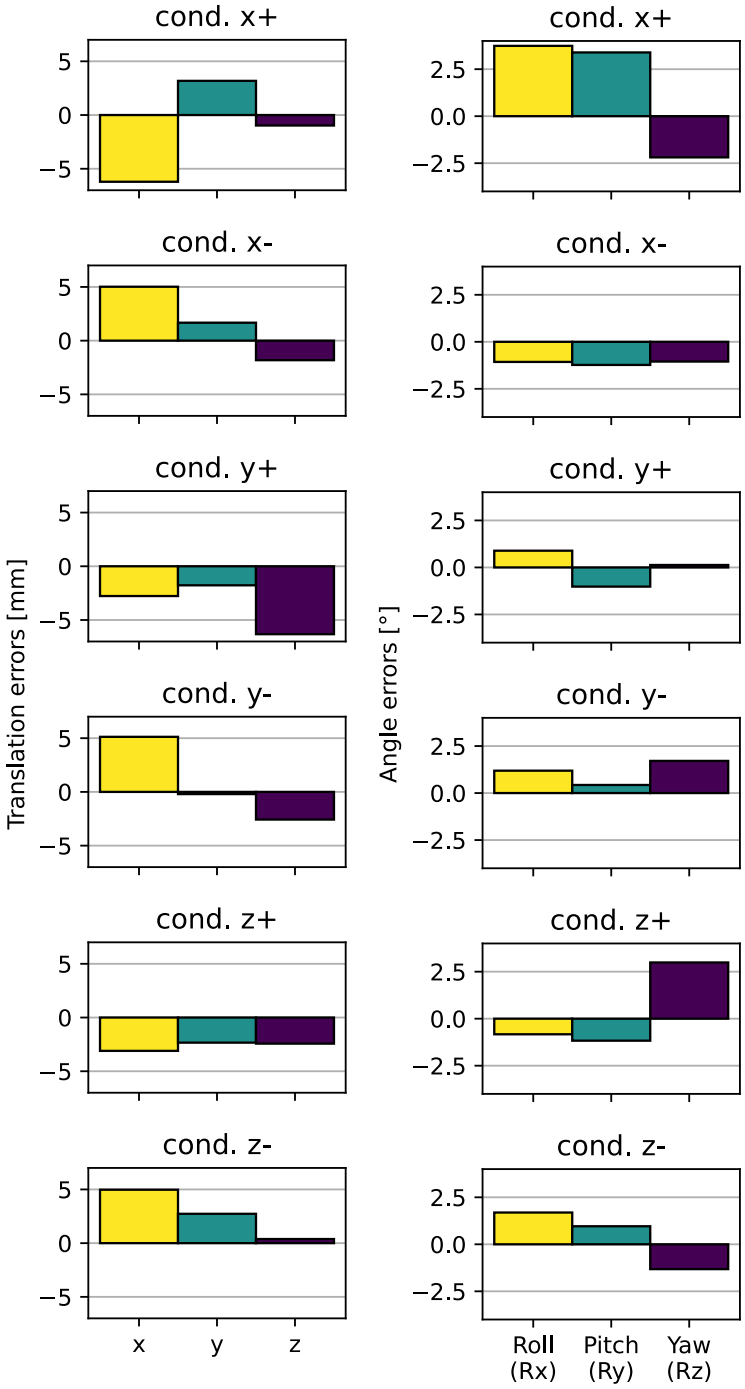

Figure 4.14 Translation and rotation errors of the platform. This figure compares the platform positioning errors obtained from simulations with those measured experimentally, across six test configurations (as listed in Tab. 1). For example, the upper left and right plots show translation and rotation errors (simulation vs experiments) for the x+ configuration, as defined in 4.1.

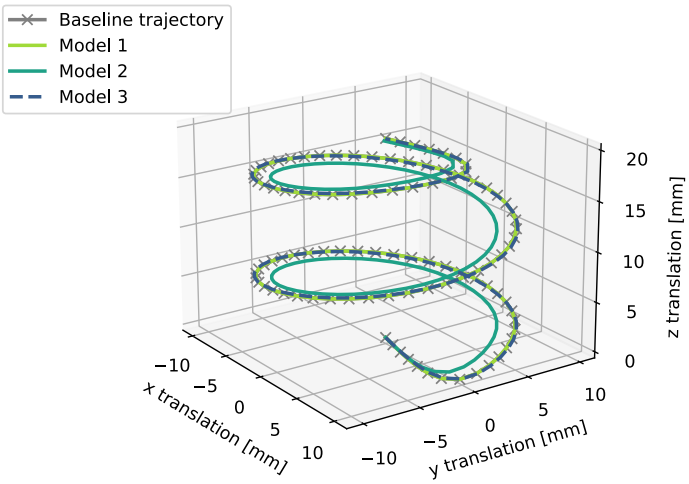

Figure 4.15 End effector trajectories from the simulation models. The figure displays the three-dimensional trajectories from the three different simulation models.

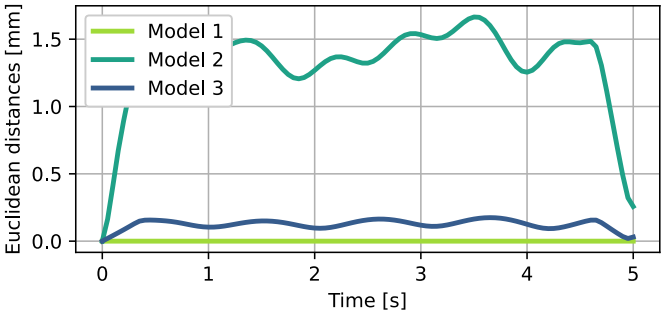

Figure 4.16 Euclidean distance errors. The figure shows the Euclidean distance errors (in millimeters) for the three different models compared to the baseline trajectory.

the "actuators") were recorded. These rotations were then inputted into the three simulation models, and the resulting output trajectories at the end-effector were recorded. The corresponding trajectories are shown in Fig. 4.15. To quantify the deviation or error between these trajectories and the reference trajectory, the Euclidean distance between corresponding points on the trajectories was computed and plotted in Fig. 4.16. This figure provides insight into the extent of deviation from the reference trajectory.

As shown, the "Fully Rigid Model" (i.e., the model with ideal revolute and spherical joints) perfectly replicates the analytically computed trajectory. The trajectory of Model 3 also closely aligns with the baseline trajectory, with the Euclidean distance error remaining low, suggesting that the cross-axis flexures provide a high degree of precision, similar to the rigid model's performance. In contrast, the model with flexible "Tetra 2" joints (Model 2) exhibits the greatest deviation from the baseline trajectory, resulting in the highest errors.

This highlights that the errors shown in Fig.4.14 are primarily due to the "Tetra 2" joints not behaving exactly like spherical joints. This points to a key design trade-off: while the use of "Tetra 2" joints is advantageous for additive manufacturing, it negatively impacts the overall motion precision of the mechanism.

4.7 Discussion

The practical implementation of this work revealed several insights that could be beneficial for further research and for other researchers.

1. As noted during the experimental investigation, the DeltaFlex demonstrated significant sensitivity to tilting moments applied to the end effector, which notably affected its ability to perform pure translations. Therefore, it is crucial to consider the impact of spurious forces and moments on parasitic motion during the design phase and to develop appropriate strategies to mitigate these effects. This study represents one of the initial attempts to experimentally explore this issue, and incorporating this evaluation in future research is recommended.

2. Another challenge encountered was the difficulty in measuring the mechanical properties of the DeltaFlex. Our initial attempt to use a high-precision coordinate measuring machine (CMM) for obtaining measurements was unsuccessful, as the force required to activate the probe was too high, causing undesired movement in the mechanism. As a result, an optical instrument (3D scanner) has been adopted to address this problem. This highlights the need for alternative contactless techniques to assess the mechanical properties of compliant robots.

3. When comparing the test and simulation data, a discrepancy in the material properties has been found, which was resolved by fine-tuning the material model in the simulations. Researchers conducting similar tests should be cautious and avoid assuming perfect accuracy in the data provided by material datasheets.

4.8 Conclusions and Future Developments

The tests conducted have provided an evaluation of the DeltaFlex's key characteristics, highlighting its low stiffness, which results in reduced resistance to motion, and its high repeatability. These findings suggest that the DeltaFlex holds promise for applications

requiring high precision and accuracy. Furthermore, the experimental results have identified areas that could benefit from optimization and improvement.

The current prototype uses stepper motors for actuation; however, future iterations could benefit from integrating low gear ratios and brushless DC (BLDC) motors. This improvement would allow for better torque control during interaction tasks, enhancing the system's precision and versatility.

Future work will focus on a comprehensive study of the flexures' fatigue life in relation to applied loads and the number of loading cycles. Additionally, exploring alternative materials and fabrication methods, such as material extrusion, could further expand the existing knowledge.

In conclusion, despite the minor challenges encountered, the methodology presented in this study offers a valuable framework for robot design, with numerous opportunities for future developments and practical applications.

Part III

Part production through Non-Planar MEX

Chapter 5

QuickCurve: revisiting slightly non-planar 3D printing

The content of this chapter has been developed during the candidate's period abroad in Nancy (France) in cooperation with the MFX laboratory

5.1 Introduction

Additive manufacturing enables the creation of 3D models by layering thin sheets of solidified material on top of one another. This technique allows the production of intricate parts without the inherent constraints associated with conventional machining methods.

However, breaking down a part into flat layers introduces the so-called *staircase effect*, which negatively impacts the surface quality and dimensional accuracy of the final components. This issue is particularly noticeable in objects printed using Material Extrusion (MEX), especially on surfaces with low curvatures. Nevertheless, MEX technology has the potential to deposit material along 3D curves, leveraging full 3-axis motion during deposition. This capability has led to a research focus on *non-planar printing*. By forming non-planar layers, these techniques seek to enhance surface quality. Some approaches even go further, proposing to use additional degrees of freedom on robotic platforms to optimise the deposition path for structural performance and support reduction (Zhang et al. (2022)).

The final part of the efforts of this thesis has been concentrated on non-planar MEX using standard 3-axis machines, aiming primarily to improve the surface quality of the top layers of a print. The advantage of 3-axis methods is that they can be readily implemented on commonly available MEX printers with minimal to no hardware changes.

The challenge of non-planar printing on 3-axis machines lies in the fixed orientation of the nozzle relative to the slope (shown in 5.1 (left)) resulting in the *gouging issue* (shown in 5.1 (right)), where the nozzle inadvertently scrapes previously deposited material due to its physical design.

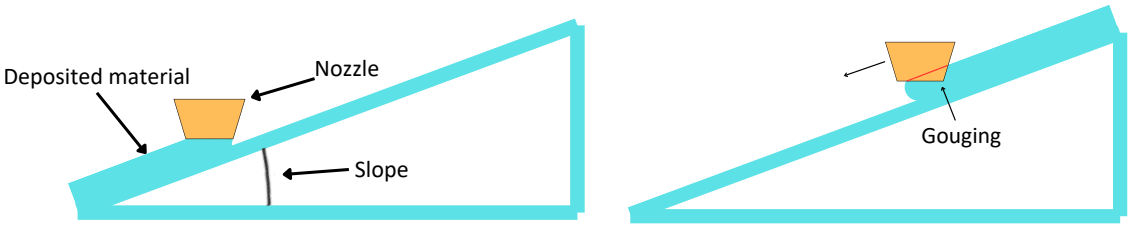

Figure 5.1 Left: the nozzle is not moving horizontally, but it is following the angle of the part's surface. Right: the nozzle scrapes the previously deposited material.

This constraint limits the maximum angle that can be effectively reproduced (Ahlers et al. (2019)). However, it's important to note that the staircase effect *becomes more pronounced at lower slopes*. Thus, even a slight degree of non-planarity can significantly enhance accuracy (Ahlers et al. (2019); Etienne et al. (2019)).

Another significant issue arising from a fixed nozzle orientation is related to the alignment of the paths with surface curvatures. A balance must be achieved in reproducing the slope, depending on the alignment of the paths with the primary curvatures. If the paths are aligned with the maximum curvature, the slopes follow the surface closely but risk substantial gouging. Conversely, aligning with the minimum curvature reduces gouging but creates a staircase pattern due to the path width across the slope. This problem has been recognised in previous studies (Ahlers et al. (2019); Song et al. (2016)), but as far as the author of this thesis knows, it has not been directly tackled. This study proposes a new strategy that aligns paths according to the principal curvatures, exploring the resulting trade-offs.

Lastly, the design of an efficient solver is emphasised. The most advanced prior methods require computationally intensive optimisation of tetrahedral meshes under inequality constraints. In contrast, the present approach necessitates only a single least-squares optimisation pass.

Contributions The present work involves:

- A highly efficient slicing algorithm optimising for a non-planar slicing surface. The geometry of this slicing surface captures the top surfaces of a model with high fidelity

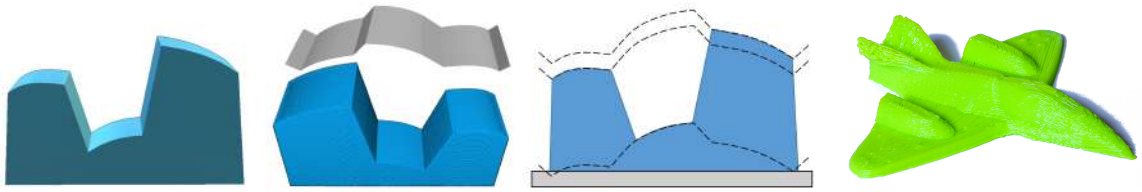

Figure 5.2 The presented method begins with a 3D model to be printed (left), using non-planar deposition to achieve an accurate top surface finish (second, bottom). The technique presented optimises a slicing surface (second, top) to extract non-planar layers (third). The rightmost image shows how the optimised slicing surface (dashed line) aligns precisely with the top surfaces, allowing a layer that follows the curvature. Additionally, a new strategy for aligning toolpaths along the curvature has been introduced. This approach allows the printing of complex parts with a non-planar surface finish (rightmost).

and ensures no collisions during fabrication. The algorithm is computationally efficient and works on the unaltered input model.

- A toolpath algorithm that aligns the paths of top surfaces according to the surface curvature, thereby enhancing surface finish by orienting deposition paths with either the maximum or minimum curvature.
- An optional filtering approach to remove minor features that could otherwise cause unwanted contours on smooth, curved surfaces. This filter is particularly effective for natural and noisy scanned surfaces, such as terrains.

These contributions collectively enable non-planar printing with low computational costs while allowing the fabrication of parts with a good quality balance, controlling how the part is divided into curved and sliced surfaces.

5.2 Method

The proposed method relies on slicing the part using a single non-planar surface. The contour of each layer is determined by intersecting the part with this slicing surface at various heights. This slicing surface is optimized to capture the curvature of the top layers while ensuring that no collisions occur. Specifically, when the slopes of the slicing surface align with those of the object's surface, the staircase defect is eliminated. An example of this alignment is shown in Figure 5.3.

The following sections detail the problem setup, the method, and its operation.

Figure 5.3 From left to right: A shape with sloped surfaces, the slicing surface optimized by the proposed method, and the resulting trajectories. All surfaces are accurately reproduced (zoom for details). Note that the vertical ridges do not interfere with curving the top surfaces.

5.2.1 Input Geometry and Output Trajectories

The method takes as input a mesh or solid definition $\mathscr{M}$. The only requirement for $\mathscr{M}$ is that it properly defines a volume, such that ray-volume intersections result in well-defined solid intervals.

The output consists of an ordered set of toolpaths, which are polylines in x, y, z (3D positions). Each vertex also has an associated attribute E that controls the amount of material extrusion from one segment to the next. All attributes are linearly interpolated during motion from one vertex to the next. These toolpaths form a continuous path in x, y, z where some segments involve no extrusion; these segments correspond to travel moves.

The goal is to optimize a slicing surface $\mathscr{S}$ defined as a height field $\mathscr{S}(x,y) : \mathbb{R}^2 \to \mathbb{R}$ above the build platform. The following sections discuss the problem formulation in terms of constraints and objectives.

5.2.2 Surface Accessibility

All surfaces with a slope[1] below a maximum angle θ_{max} can be accessed by the nozzle without causing self-collisions. This is based on the conical collision model of the nozzle (Ahlers et al. (2019); Etienne et al. (2019); Ezair et al. (2018)).

A valid slicing surface is therefore defined as a continuous surface where the slope everywhere is below θ_{max}. Such a surface has a bounded gradient (Etienne et al. (2019)) and guarantees that the part can be fabricated under the conical collision model. During fabrication, the slicing surface separates the already printed layers below from the layer currently being printed. Since all print trajectories for a layer follow the slicing surface, and this surface is itself collision-free, no collisions will occur.

[1] Slope is measured as the angle between the surface gradient and the horizontal plane; for instance, the XY plane has a zero slope.

It should be noted that for some printers, the conical model may not be sufficient because the extrusion device body could be positioned close to the nozzle tip (Ahlers et al. (2019)). For simplicity, this is not considered here, but in practice, the maximum slope can be adjusted to account for the extruder body.

5.2.3 Slope Control

The method is controlled by an input map $\Theta : \Omega \to \mathbb{R}$, where $\Omega \subset \mathbb{R}^2$. This map specifies the desired shape of the surfaces to be fabricated at selected x, y locations, represented as connected pieces of height fields. The slope at a point x, y in Ω is given by $\theta(\Theta(x,y))$, calculated using finite differences in Ω.

The map must be defined such that at every point in Ω, the condition $\theta(\Theta(x,y)) < \theta_{max}$ is satisfied. This angle is shown in 5.4 (left). For simplicity, $\theta(\Theta(x,y))$ will often be referred to as simply θ when context allows.

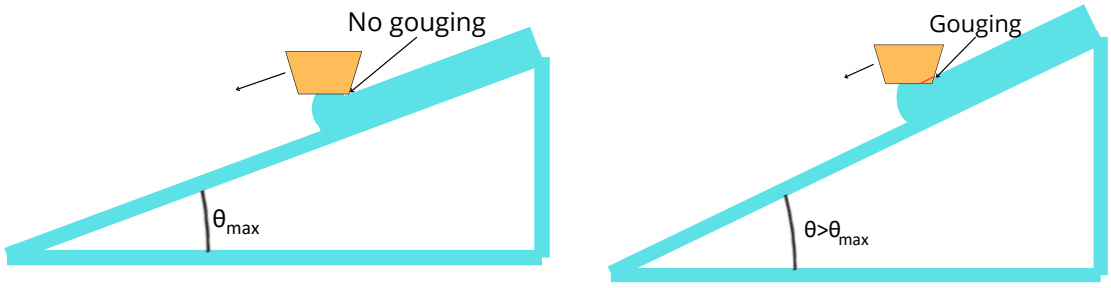

Figure 5.4 Left: the angle is such that the upper part of the previously deposited material and the nozzle are tangent. In this case, there is no gouging issue. Right: the angle exceeds the maximum, and the gouging issue occurs.

Θ is typically a sparse map, specifying the target surfaces only at selected locations. In the examples, Θ is obtained by selecting the top surfaces of $\mathscr{M}$ (viewed from above) that have a slope below a user-defined target maximum slope $\theta_{target} < \theta_{max}$. However, users can also directly specify the map, or it can be optimized using another algorithm; the surfaces in Θ do not necessarily need to be a subset of those in $\mathscr{M}$.

It is important to distinguish between θ_{max} and θ_{target}. θ_{max} ensures safe fabrication without collisions (5.4 (right))3 263, whereas θ_{target} reflects user preference. Due to nozzle gouging, it is often undesirable to curve everything below θ_{max}; instead, a balanced approach is often better.

5.2.4 Slice Optimization

The algorithm aims to optimise a slicing surface that divides $\mathscr{M}$ into a set of layers. The primary goal is for the slicing surface to accurately reproduce the surfaces specified in Θ. This is achieved when, during slicing, the slicing surface aligns precisely with the shape of each surface in Θ (Figure 5.5, right). It's important to note that the absolute altitudes of the surfaces are not critical; it is sufficient for the slicing surface to align with the target surface at some height. This key insight forms the basis of the optimization process.

The slicing surface must also be *valid* to ensure proper fabrication. In the optimisation step, slice validity is treated as an objective and is later enforced as a post-process (Section 5.2.5).

The slicing surface $\mathscr{S}$ is optimised as a discrete height field. The optimization variables are a set of displacements (or altitudes) from the printing bed, denoted as $h_{(i,j)}$ where i, j are indices in the 2D discretized version of $\mathscr{S}$. The degrees of freedom are the altitudes where a target surface is *not* defined in the control map Θ. Where Θ is defined, the slicing surface is constrained to follow the provided surfaces.

A reasonable objective for filling in the free regions around the surfaces in Θ would be to make the slicing surface as smooth as possible in those areas. However, as shown in Figure 5.5 (left), the top surfaces (in green) may be separated by a large vertical distance while being relatively close in the x, y plane. Consequently, it is not possible to create a smooth slicing surface with a slope everywhere below θ_{max}. This is the main challenge in curving the middle surface in Figure 2.1.

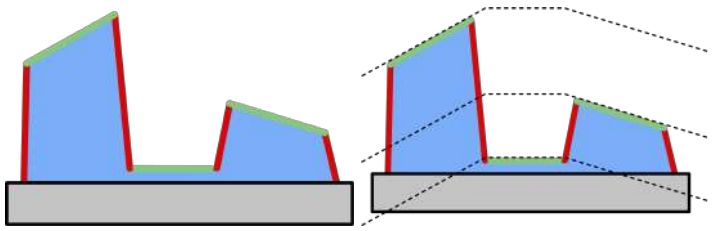

Figure 5.5 Left: The green surfaces are specified in Θ, while the red ones are left free because their slopes exceed θ_{target}. The relative heights of the green surfaces make it impossible to find a slicing surface with slopes everywhere below θ_{max}. Right: By allowing the green surfaces to "float" up and down during optimization, the approach computes the dashed line as the slicing surface, which accurately reproduces all surfaces in Θ.

To solve this problem, additional variables are introduced, one for each connected component in Θ. These variables allow each target surface to move vertically, effectively "floating" up or down. Let $\mathscr{C}$ denote the set of connected components in Θ. Each component

$c \in \mathscr{C}$ is associated with a variable z_c. The values of $h_{(i,j)}$ within a component c are fully determined by z_c as $h_{(i,j)} = z_c + \Theta(i,j) - \Theta(c_0)$, where c_0 is a reference point arbitrarily chosen in c.

Each free variable that neighbors a connected component is required to match the height of its neighbor. Specifically, for a coordinate i, j in component c with a free neighbor $h_{(i,j)+\delta}$, where $\delta \in [-1,1]^2$, the objective is set such that $h_{(i,j)+\delta} = z_c + \Theta(i,j) - \Theta(c_0)$.

Within the free regions, the slicing surface gradient is encouraged to *steepen*. This is based on the observation in Etienne et al. (2019) that surfaces should either be exactly curved or sliced at an angle as perpendicular as possible to the surface. For a free coordinate i, j with a free neighbor $(i,j)+\delta$, where $\delta \in [-1,1]^2$, the objective is defined as:

$$h_{(i,j)} - h_{(i,j)+\delta} = H_{target} \quad \text{if } \Theta(i,j) > \Theta((i,j)+\delta)$$
$$h_{(i,j)+\delta} - h_{(i,j)} = H_{target} \quad \text{otherwise}$$

where H_{target} is computed from θ_{target} based on the chosen discretization step of S (typically $50\mu m$). This formulation increases the local gradient to match the selected target slope.

These equations optimise the free variables $h_{(i,j)}$ and z_c to produce a surface with the desired gradient. This results in a least-squares problem similar to solving the Poisson equation on a grid (Pérez et al. (2003)), adding per-component variables. The solution is obtained using the Eigen library (Guennebaud et al. (2010)).

An initial result is presented in Figure 2.1 for the shape depicted in Figure 2.1. A half-cylinder model is illustrated in Figure 5.6, where only the top portion of the cylinder can exhibit curvature. Due to gradient steepening, the slicing surface adopts an orthogonal orientation relative to the remaining surface, enhancing the quality of the slicing process.

Although this approach frequently yields a valid slice, it does not ensure one in all cases. The geometry of the constraint surface and their specific positions within Θ can sometimes prevent finding a feasible solution. Rather than depending on inequality constraints and a more complicated solver, a post-processing method that effectively addresses sparse constraint violations is suggested.

5.2.5 Post-processing

The optimizer may produce a surface where the slope exceeds θ_{max} in certain areas. This occurrence is generally infrequent when θ_{target} is set well below θ_{max}, but it becomes more problematic as θ_{target} approaches higher values. An illustration of this is provided in Figure 5.7.

The presented post-processing technique adjusts the slice surface to ensure the constraints are met throughout. The algorithm scans the surface from top to bottom, visiting all altitudes

Figure 5.6 Top: Half a cylinder (left) and the trajectories produced by the presented technique (right). Note the curved top. Bottom: Showing half of the bottom layers (left) reveals the shape of the slicing surface (right).

in $\mathscr{S}$ in descending order, and incrementally modifies the surface. This approach is inspired by the algorithm proposed by Hornus et al.(Hornus and Lefebvre (2018)) for creating cavities with specific angles within parts.

Consider a specific height h and the current surface $S_{h+\Delta}$, where $h+\Delta$ represents the previous height. Without loss of generality, assume that the height h is present only at a particular point p (this is done iteratively for all points). The surface S_h is derived from $S_{h+\Delta}$ by updating the surrounding locations around p as follows: $S_h(p) = \max_{\delta \in [-1,1]^2}(S_{h+\Delta}(p+\delta) - H_{max}, S_{h+\Delta}(p))$, where H_{max} denotes the maximum permissible height difference between neighboring points on the map (Section 5.2.4). This operation propagates the angular constraint from the top downwards, correcting areas that would otherwise violate the conical constraint.

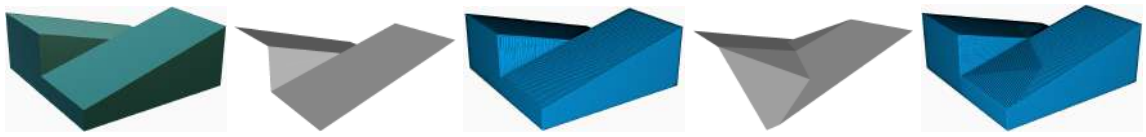

Figure 5.7 Shape to be sliced, Optimized slice surface (the vertical ridge violates θ_{max}), The resulting GCode cannot be printed safely, The corrected slice surface (the angle everywhere complies with θ_{max}), The resulting GCode (note how parts of the surfaces are now sliced to avoid collisions).

5.2.6 Slicing and toolpath orientation

The slicer utilizes a ray-representation approach. Rays are projected from above through the part $\mathscr{M}$, generating a series of solid and empty segments along each ray's path. When performing standard slicing, contours are determined by identifying which rays are solid at a specific slicing height. This method allows for an easy transformation of the slice shape from a planar configuration to a height field by adjusting the intervals along the rays in accordance with $\mathscr{S}$.

Once the slice contour is generated, it is initially treated as flat. The 2D outline is then filled with toolpaths, which are subsequently deformed back to the original geometry following methods similar to those in previous studies (Ahlers et al. (2019); Etienne et al. (2019)).

However, unlike previous approaches, the toolpaths generated here are designed to cover the surface based on its curvature. This work extends the method proposed by Chermain et al. (Chermain et al. (2023)), which generates orientable trajectories for fabricating anisotropic appearances. In this context, the direction field is defined by the curvature in Θ. The implementation closely follows the phasor optimization and trajectory extraction techniques described in their study.

The direction of the paths is constrained along the boundary of Θ and on a coarse internal grid (spaced every 3 mm) to provide some flexibility to the orientation optimizer within these regions. Outside these constraints, the direction is left unrestricted. Additionally, in flat regions of Θ (where the angle is close to zero), the orientation remains free. The phase is constrained at least at one point, and it is varied by an angle of $\frac{\pi}{4}$ with each layer to create a staggered pattern.

This approach enables the creation of fully filled curved surfaces where the path orientation is carefully controlled. Two main orientation strategies in relation to the curvature are primarily explored. The first strategy aligns the paths along the direction of maximum principal curvature. This reduces the formation of stair-step artifacts across the path widths by ensuring that the paths follow the main slope's upward and downward movement. This is the preferred approach when aiming to achieve a fully curved surface.

The second strategy orients the paths along the direction of minimum principal curvature, causing the paths to generally cross the main slope. This option is particularly effective for curved surfaces with gentle slopes that transition to areas printed in a non-planar manner. Figure 5.8 demonstrates the method in a simple scenario, and several examples of both strategies are provided in Section 5.3, where the technique is applied to various prints.

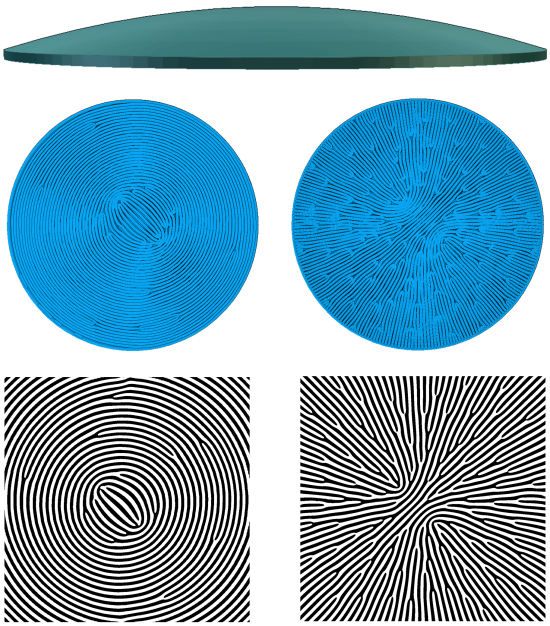

Figure 5.8 Top: A curved dome. Middle: The produced trajectories. Bottom: The optimized phasor fields (Chermain et al. (2023)).

5.2.7 Filtering

Certain shapes, such as scanned 3D models or those affected by tessellation artifacts, often exhibit noisy surfaces and minor triangulation defects. These imperfections can result in isolated islands that generate unintended contours on an otherwise smooth surface, as shown in Figure 5.9. This issue is particularly challenging when the size of these defects is comparable to the deposition width, making them difficult to accurately capture.

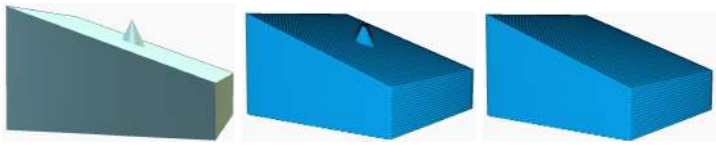

Figure 5.9 Illustration of filtering on a test case. This model (left) contains a spike preventing a fully curved surface (middle). This is akin to noise in scanned or natural shapes. The adopted filter allows the removal of these tiny features, preserving the smoothness of the original surface (right).

To address these 'holes,' a morphological closure is applied to the connected components of Θ, with each closed region being labelled. During the optimization of the slicing surface, gradient steepening is disabled in these tagged regions, focusing instead on achieving smoothness. During the slicing process, the top of the shape within each closed region is snapped to

perfectly align with the slicing surface, thereby eliminating the unwanted geometry these features might otherwise introduce.

A single parameter controls this filtering process, the closure radius ρ. While optional, this filter proves to be particularly valuable in practice for organic or natural shapes, as illustrated in Figure 5.10. For mechanical or geometrically regular parts, using a small filter with a radius corresponding to the deposition width ($\rho = 0.2$mm) effectively removes small regions caused by tessellation and discretization noise. The choice of this parameter is specified in all results where it is set to a non-zero value. Additionally, a graphical user interface (GUI) could be easily designed to allow users to selectively apply this filter.

Figure 5.10 Illustration of filtering on a real case. This terrain model (Figure 5.11) has a slight noise on its surface producing tiny features and spurious contours atop the main curved region. From upper-left to lower-right the filter radius is respectively $\rho = 0$, $\rho = 1$, $\rho = 2$, $\rho = 3$ mm. The presented filter cleans up most of these issues. It is, however, a compromise as it modifies the geometry; for instance, an overly aggressive filter (rightmost) removes the dent along the front edge from the geometry.

The map in Figure 5.11 shows the various ingredients used on the landscape model, next to the model itself.

5.3 Results

This section presents additional 3D printed results, explores various trade-offs, and provides comparisons with existing methods.

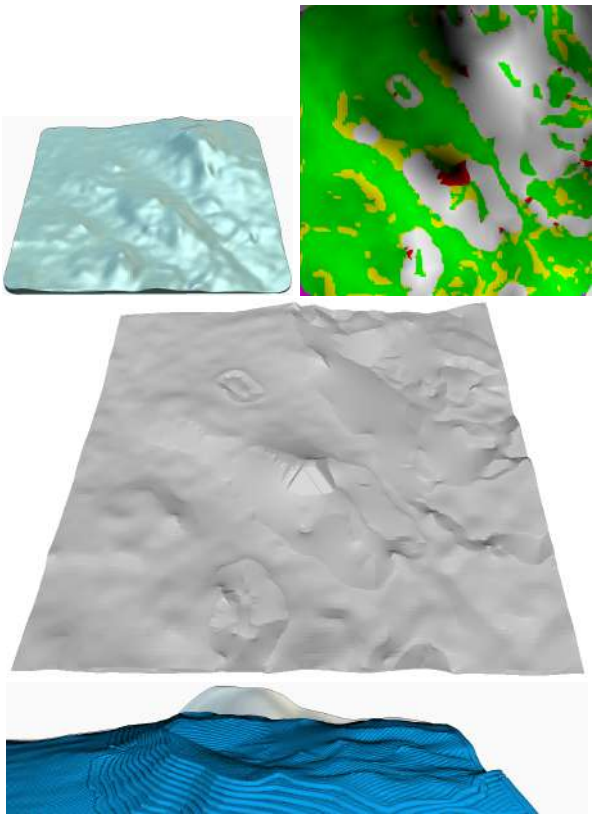

Figure 5.11 At the top, the terrain model (top left) and a map of the various ingredients being used in various locations (top right). In green the target surface of Θ, in yellow the areas impact by the filter ($\rho = 2$mm), in red the regions modified by the post-process (Section 5.2.5). In the middle, the final slicing surface. The produced trajectories are visible in Figure 5.10, third from the left. At the bottom, a close up of the mountains without the top layers, revealing the effect of gradient steepening: the interior is concave.

5.3.1 Printed results

A delta printer with a nozzle providing additional clearance is utilized, both of which are standard and commercially available. Printing is done using PLA material with 1.75mm filament, and the nozzle extrudes with a standard diameter of 0.4mm.

Figure 5.12 provides a detailed analysis of different trade-offs for printing a terrain model, illustrating how aligning the orientation to the curvature can enhance surface finish quality, particularly on gently sloped surfaces. However, the close-up view reveals that the tall mountain section is prone to gouging at its steepest points, where traditional layers offer better results. The final result (rightmost) demonstrates how the proposed method achieves a balanced compromise. In this case, orienting the paths along the direction of minimal curvature results in a smoother transition at the mountain's base. Even though the mountain

is sliced, it does not involve flat slicing and benefits from gradient steepening, as further illustrated in Figure 5.11, bottom.

Figure 5.13 presents a Zelda-themed badge, comparing a standard print with the proposed method. The comparison highlights a significant improvement in surface quality at the top and shows how the trajectories naturally follow the slope (orientation along maximum curvature).

Figure 5.14 provides another example of balancing between sliced and curved surfaces. While both non-planar results show marked improvements on the slightly sloped sections, the fully curved result experiences significant gouging near the heel. The final version effectively captures all parts of the insole, providing a uniformly smoother texture throughout.

Figure 5.15 illustrates trajectories optimized along the maximum principal curvature of a shield model, enabling curved printing on all surfaces, including the interior circular grooves. Figure 5.16 displays a preview of the trajectories for the jet model featured in the teaser (Figure 5.2). Figure 5.17 showcases a climbing knob model with curved top surfaces.

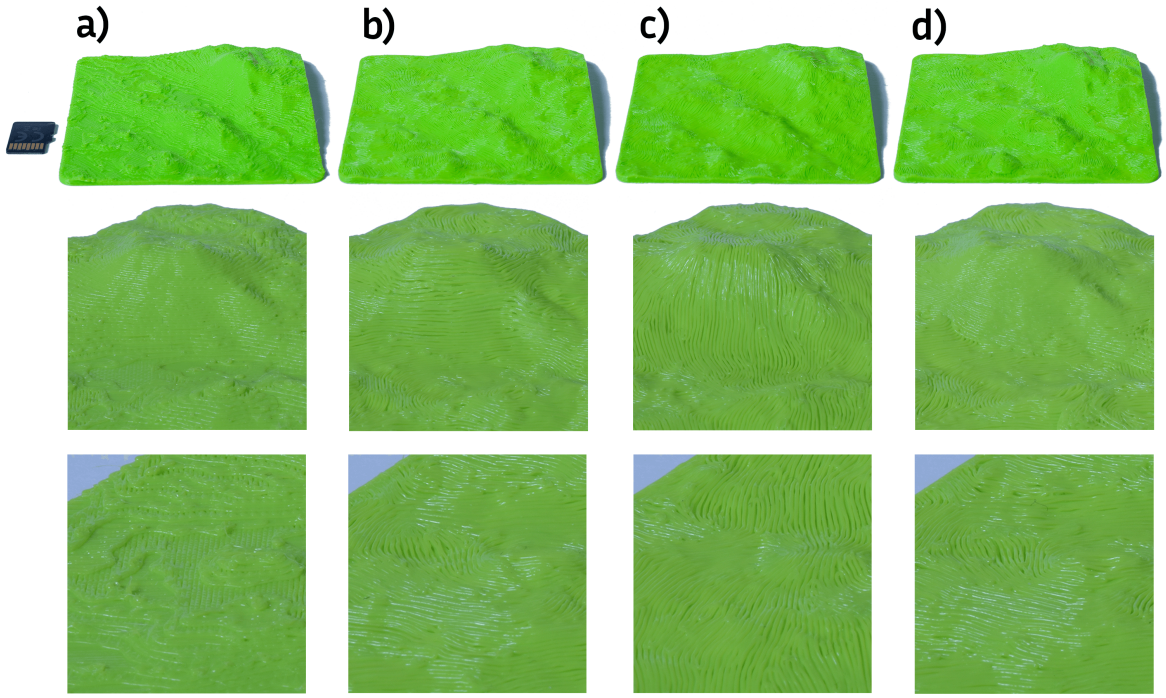

Figure 5.12 *Billinge terrain model.* a) Planar print, b) fully curved print with orientation along the minimum principal curvature, c) fully curved print with orientation along the maximum principal curvature, d) curved print with a reduced target angle to achieve a balance and minimize gouging. The first row of close-ups highlights the mountains, while the second row emphasizes a gently sloped area. (Zoom in for detailed views).

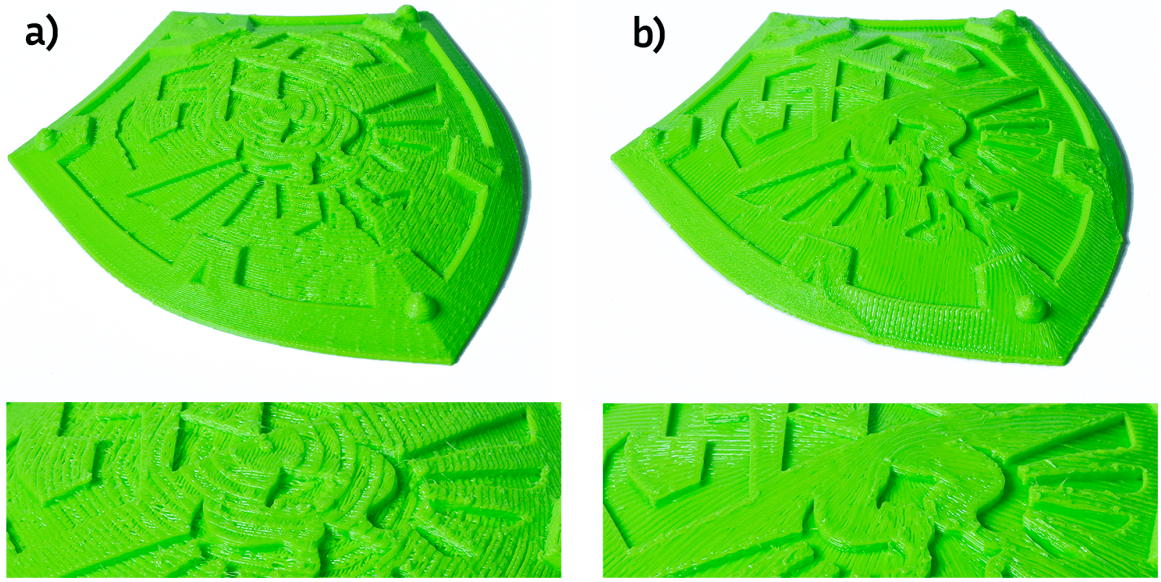

Figure 5.13 *Zelda shield model*. a) Planar print. b) Non-planar print with a compromise between curving and steepening ($\theta_{target} = 27°$, $\rho = 0.5$mm). The orientation follows the maximum principal curvature. (Zoom to reveal details).

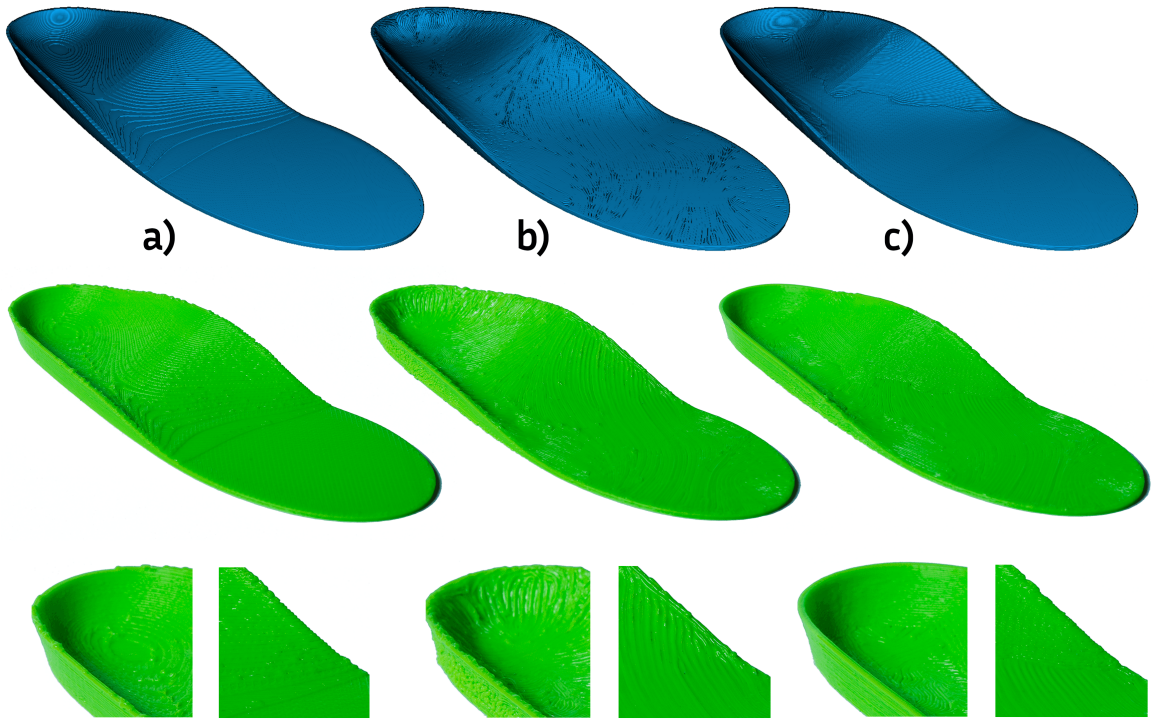

Figure 5.14 *Insole model*. a) Planar print. b) Fully non-planar print, note the gouging towards the heel. c) Non-planar with a compromise between curving and slicing ($\theta_{target} = 27°$, $\rho = 0.5$mm). On both b) and c) the orientation follows the maximum principal curvature. (Zoom in for details).

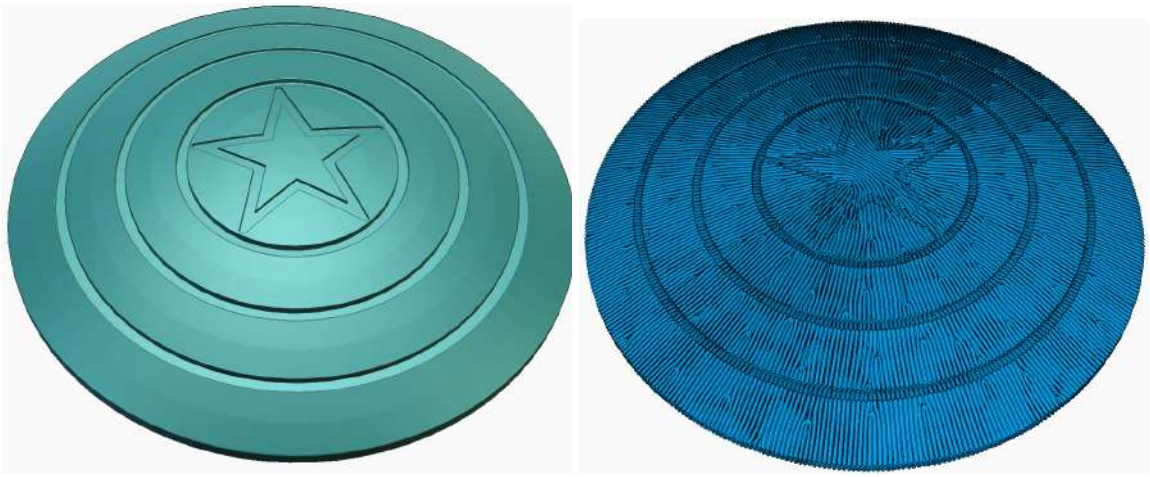

Figure 5.15 *The Captain's shield*. A round shield model and the paths generated along the maximum curvature.

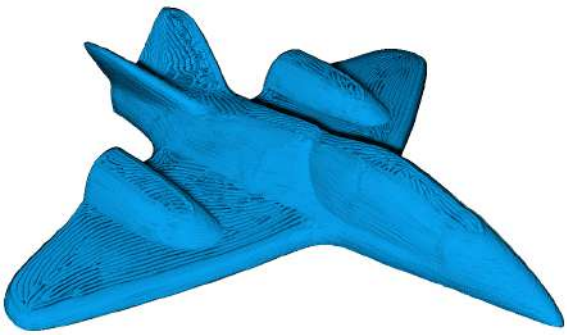

Figure 5.16 *Jet*. The trajectories of the jet model shown in Figure 5.2, rightmost.

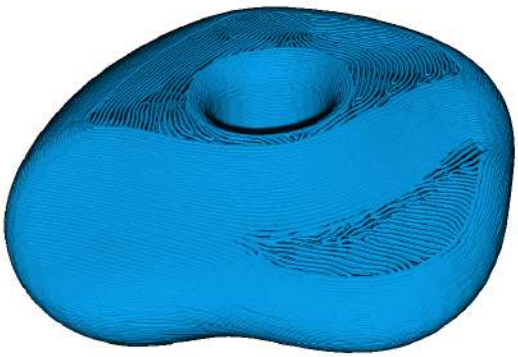

Figure 5.17 *Climbing knob*. The trajectories of a climbing know model, note how two top surfaces are curved and separated by sliced surfaces.

5.3.2 Comparisons

The comparison focuses on CurviSlicer (Etienne et al. (2019)) and the method developed by Ahlers et al. (Ahlers et al. (2019)). For both methods, the publicly available implementations provided by the original authors on GitHub are utilized. All methods are configured with matching parameters for sloping constraints and slicing settings.

The analysis begins by comparing the computation times between CurviSlicer (Etienne et al. (2019)) and the proposed method, using several test parts featured either in this work or in Etienne et al. (2019). The results are summarized in Table 5.1. The tests were conducted on a computer with an Intel(R) Core i7-11800H CPU (3.80 GHz), 16 GB of RAM, and an integrated Intel UHD Graphics GPU.

The results show that the slicing optimizer significantly outperforms CurviSlicer. In some cases, CurviSlicer failed to produce a result (e.g., Jet, Insole, Billing). Although the proposed approach is generally much faster, there is a notable overhead associated with using the path orientation optimizer (*optizor*). Consequently, the total computation time can be higher due to the chosen path orientation strategy. Currently, the orientation optimizer is applied uniformly to every layer, even though it is most effective on the top layers. Additionally, the computation cost can vary greatly depending on the GPU, and these tests were conducted on a low-power laptop GPU.

	Curvislicer				QuickCurve Standard toolpaths			QuickCurve Optizor toolpaths		
	Tetrahed--ralization [s]	Slicing + paths [s]	Optim. [s]	Total [s]	Curved slicing preparation [s]	Slicing + paths [s]	Total [s]	Curved slicing preparation [s]	Slicing + paths [s]	Total [s]
Car model	331.2	0.6	493.7	**871.7**	6.7	0.5	**19.2**	7.1	0.5	38.8
Dome	66.8	0.5	363.3	**436.9**	3.1	0.5	**25.6**	3.0	0.4	38.2
Robotic ankle	62.5	0.6	46.3	118.9	27.3	0.5	**69.6**	31.0	0.4	**423.8**
Jet	186.8	N/A	N/A	N/A	57.8	0.5	**84.8**	78.6	0.4	269.8
Insole	74.8	N/A	N/A	N/A	7.4	0.4	**28.1**	7.4	0.5	100.1
Cheese stopper	295.7	0.6	1612.9	**1942.8**	7.4	0.4	**51.8**	6.5	0.4	153.3
Wing	19.8	0.6	4.9	31.0	2.2	0.4	**23.1**	2.1	0.4	**274.3**
Eggs box	595.0	0.6	698.2	1347.3	11.5	0.4	**86.5**	12.1	0.5	**1307.4**
Foil cutter	40.9	0.5	400.9	**448.5**	5.1	0.4	**26.3**	5.0	0.5	55.3
Billinge	355.6	N/A	N/A	N/A	2.2	0.5	**34.1**	3.2	0.5	60.0
Link's shield	N/A	N/A	N/A	N/A	45.0	0.5	**92.1**	49.3	0.5	224.8

Table 5.1 This table shows a time comparison between Curvislicer Etienne et al. (2019) and the presented method. For the one discussed here, two versions are measured: standard toolpath generation and orientation optimized paths (*optizor*). The different steps of the algorithms are broken down, highlighting in green the fastest times and in red the slowest.

The algorithm by Ahlers et al. (Ahlers et al. (2019)) is extremely fast due to its lack of optimization steps. However, it is less versatile, as illustrated in Figure 2.1. Furthermore, in several tests, the implementation failed to generate any curved layers, particularly for the insole and jet models. While this might be due to an implementation issue, it also stems from

the fact that any collision results in the exclusion of an entire surface from being curved, which can be quite restrictive for complex surfaces.

A new approach here strikes a different balance between generality and computational efficiency. This method is faster and simpler to implement than optimizing for a full volume deformation, as seen in Etienne et al. (2019), while being more adaptable than methods that only curve fully accessible top surfaces (Ahlers et al. (2019)). Additionally, two novel elements are introduced: 1) A filtering mechanism to eliminate unwanted small features within otherwise smoothly curved regions, which is particularly useful for scanned or natural surfaces. 2) A path orientation strategy that provides the flexibility to align paths along either the maximum principal curvature, the minimum principal curvature, or any angle in between. Aligning paths with the maximum curvature helps avoid staircase defects caused by paths crossing the curvature, while aligning with the minimum curvature allows for smoother transitions between curved and planar sections of a print.

Limitations and Future Work. The proposed technique has several limitations, which also suggest directions for future research.

In terms of versatility, the current method only considers the top surface, whereas the volume-based approach in Etienne et al. (2019) can curve surfaces throughout the entire part. Regarding optimization, the path orientation optimizer is currently applied at every slice to achieve solutions with varying phases (and thus alignments). This introduces a computational cost that is likely only warranted for the visible layers. To address this, a modification is planned for the slicer to use standard zigzag infills internally and optimize orientations only on the top layers.

There is potential to adapt this technique for multi-axis robotic platforms, where the nozzle can be tilted. In such contexts, the gouging issue is less critical, and the orientation of paths within layers could be further optimized to meet structural requirements (Fang et al. (2020); Zhang et al. (2022)).

Part IV

Conclusions

Chapter 6

Conclusions

6.1 Summary

This dissertation addresses the adoption of AM for the fabrication of high-performance components, focusing on two main aspects: the change of perspective related to the design and the manufacturing process. Specifically, it explores the development of monolithic with compliant joint mechanisms, highlighting their associated benefits, and investigates the implementation of non-planar Material Extrusion. The research activities were divided into two main parts as summarized below.

6.1.1 Monolithic mechanisms with compliant joints

With the vision of advancing robotic mechanisms through AM, detailed design analyses of two monolithic systems employing compliant joints were conducted. A compliant monolithic gripper and a compliant monolithic delta robot were developed and evaluated, emphasising the advantages of such designs.

A CAD-based approach was employed to model and simulate the behavior of the gripper (Chapter 2) and the delta robot (Chapter 3). The gripper design highlights benefits such as reduced weight, faster production, and time savings due to the elimination of assembly processes. Similarly, the delta robot showcases the efficiency and performance gains achievable with monolithic structures. Both systems underline the potential of compliant joints in enhancing functionality while simplifying production, demonstrating the promise of this design approach for advanced robotic applications.

6.1.2 Non-planar MEX algorithm

To advance the capabilities of desktop additive manufacturing systems, a novel algorithm for non-planar Material Extrusion (MEX) was developed. This approach enables the production of parts with superior aesthetic and functional characteristics, leveraging the accessibility of widely available low-cost AM machines.

The algorithm utilises the surface of the part itself as the slicing one, allowing toolpaths to closely follow the contours of the geometry. This method effectively reduces or eliminates the staircase effect for a wide variety of shapes. Furthermore, the algorithm is designed to avoid gouging wherever possible, ensuring the quality and accuracy of the printed parts. Its computational efficiency and speed make it an ideal solution for enhancing surface quality without compromising accessibility or affordability.

6.2 Contributions

The above mentioned research activities, in part, resulted into the following list of scientific publications:

1. E. Ottonello, M. Baggetta, G. Berselli and A. Parmiggiani, "Design and Validation of a Push-Latch Gripper Made in Additive Manufacturing," in IEEE/ASME Transactions on Mechatronics, vol. 28, no. 4, pp. 2083-2091, Aug. 2023, doi: 10.1109/TMECH.2023.3276073.

2. Parmiggiani, A., Ottonello, E., Kargar, S. M., Baggetta, M., Hao, G., and Berselli, G. (July 22, 2024). "DeltaFlex—An Additively Manufactured Delta Robot With Compliant Joints: Virtual Prototyping and Experimental Evaluation." ASME. J. Mechanisms Robotics. November 2024; 16(11): 111011. 10.1115/1.4065780

3. Ottonello, E., Hugron, P.-A., Parmiggiani, A., and Lefebvre, S. (2024). Quickcurve: revisiting slightly non-planar 3d printing. ArXiv. June 2024. doi: 10.48550/arXiv.2406.03966

6.3 Outlook

This dissertation has explored the potential of additive manufacturing in developing high-performance components with a focus on two key innovations: monolithic mechanisms featuring compliant joints and non-planar MEX for desktop fabrication.

Monolithic mechanisms, fabricated as single, integrated units, demonstrated significant advantages in terms of design and production. The use of compliant joints enhanced their robustness, reduced maintenance needs, and allowed for smooth elastic deformations. By eliminating the need for assembly, these mechanisms achieved improved structural integrity, reduced weight, and greater manufacturing efficiency. Applications in robotic systems, such as the compliant gripper and delta robot designs presented, highlighted the practical benefits of this approach, showcasing reduced costs and increased reliability in industrial applications.

On the other hand, the development of a novel algorithm for non-planar MEX introduced a transformative approach to additive manufacturing. The algorithm enabled the use of desktop machines to produce parts with exceptional surface quality by aligning the slicing planes with the curved geometries of the models. This technique minimised the staircase effect, delivering smooth surfaces directly from the printer and reducing the need for post-processing. Additionally, the algorithm's computational efficiency ensured rapid and accessible deployment, while its ability to prevent gouging maintained the integrity of complex geometries.

Together, these innovations exemplify how AM technologies can bridge the gap between theoretical potential and practical applications. By integrating advanced design methodologies and optimizing manufacturing processes, this research is a starting point for more efficient, cost-effective, and versatile solutions in robotics and industrial domains. Future work may focus on further refining these technologies and expanding their scope to include new materials, geometries, and application areas.

References

(2023). *Conceptual Design and Virtual Prototyping of a Compliant, Low-Cost Prosthetic Hand*, volume ASME 2023 Conference on Smart Materials, Adaptive Structures and Intelligent Systems of *Smart Materials, Adaptive Structures and Intelligent Systems*.

(Visited on: 2023-01-10). Automation technology and technical education solutions | Festo GB.

(Visited on: 2023-01-10). BTM Europe - State of the Art Clinching Systems.

(Visited on: 2023-01-10). Schunk.

Ahlers, D., Wasserfall, F., Hendrich, N., and Zhang, J. (2019). 3d printing of nonplanar layers for smooth surface generation. In *2019 IEEE 15th International Conference on Automation Science and Engineering (CASE)*, pages 1737–1743.

Akhoundi, B., Jahanshahi, A. S., and Abbassloo, A. (2024). G-code generation for deposition of continuous glass fibers on curved surfaces using material extrusion-based 3d printing. *Engineering Research Express*, 6(1):015401.

Allen, R. J. and Trask, R. S. (2015). An experimental demonstration of effective curved layer fused filament fabrication utilising a parallel deposition robot. *Additive Manufacturing*, 8:78–87.

Bi, D., Duan, M., Lau, T. Y., Xie, F., and Tang, K. (2023). Strength-enhanced volume decomposition for multi-directional additive manufacturing. *Additive Manufacturing*, 69:103529.

Bilancia, P. and Berselli, G. (2021). An overview of procedures and tools for designing nonstandard beam-based compliant mechanisms. *Computer-Aided Design*, 134:103001.

Bilancia, P., Berselli, G., Bruzzone, L., and Fanghella, P. (2019). A CAD/CAE integration framework for analyzing and designing spatial compliant mechanisms via pseudo-rigid-body methods. *Robotics and Computer-Integrated Manufacturing*, 56:287–302.

Birglen, L. and Schlicht, T. (2018). A statistical review of industrial robotic grippers. *Robotics and Computer-Integrated Manufacturing*, 49:88–97.

Brown, E., Rodenberg, N., Amend, J., Mozeika, A., Steltz, E., Zakin, M. R., Lipson, H., and Jaeger, H. M. (2010). Universal robotic gripper based on the jamming of granular material. *Proceedings of the National Academy of Sciences*, 107(44):18809–18814.

Bruyas, A., Geiskopf, F., Meylheuc, L., and Renaud, P. (2014). Combining multi-material rapid prototyping and pseudo-rigid body modeling for a new compliant mechanism. In *2014 IEEE International Conference on Robotics and Automation (ICRA)*, pages 3390–3396.

Bruyas, A., Geiskopf, F., and Renaud, P. (2015). Design and modeling of a large amplitude compliant revolute joint: The helical shape compliant joint. *Journal of Mechanical Design*, 137:085003.

Bárnik, F., Vaško, M., Handrik, M., Dorčiak, F., and Majko, J. (2019). Comparing mechanical properties of composites structures on onyx base with different density and shape of fill. *Transportation Research Procedia*, 40:616–622. TRANSCOM 2019 13th International Scientific Conference on Sustainable, Modern and Safe Transport.

Chakraborty, D., Aneesh Reddy, B., and Roy Choudhury, A. (2008). Extruder path generation for curved layer fused deposition modeling. *Comput. Aided Des.*, 40(2):235–243.

Chen, B., Shao, Z., Xie, Z., Liu, J., Pan, F., He, L., Zhang, L., Zhang, Y., Ling, X., Peng, F., Yun, W., and Wen, L. (2021). Soft origami gripper with variable effective length. *Advanced Intelligent Systems*, 3(10):2000251.

Chermain, X., Zanni, C., Martínez, J., Hugron, P.-A., and Lefebvre, S. (2023). Orientable dense cyclic infill for anisotropic appearance fabrication. *ACM Trans. Graph. (Proc. SIGGRAPH)*, 42(4).

Clavel, R. (1987). Device for displacing and positioning an element in space, WIPO Patent WO1987003528A1.

Correa, J. E., Toombs, J., Toombs, N., and Ferreira, P. M. (2016). Laminated micro-machine: Design and fabrication of a flexure-based delta robot. *Journal of Manufacturing Processes*, 24(5):370–375.

Dai, C., Wang, C. C. L., Wu, C., Lefebvre, S., Fang, G., and Liu, Y.-J. (2018). Support-free volume printing by multi-axis motion. *ACM Trans. Graph.*, 37(4).

Deimel, R. and Brock, O. (2013). A compliant hand based on a novel pneumatic actuator. In *2013 IEEE International Conference on Robotics and Automation*, pages 2047–2053.

Do, T. V., City, H. C. M., Viet, N. Q., Nam, N. Q., Dat, P. N., Vinh, D. D., and Hung, T. V. (2021). Design of delta robot using image processing for product sorting process. In *2021 International Conference on System Science and Engineering (ICSSE)*, pages 210–214, Nha Trang City, Vietnam.

Drotman, D., Jadhav, S., Karimi, M., de Zonia, P., and Tolley, M. T. (2017). 3D printed soft actuators for a legged robot capable of navigating unstructured terrain. In *2017 IEEE International Conference on Robotics and Automation (ICRA)*, pages 5532–5538.

Etienne, J., Ray, N., Panozzo, D., Hornus, S., Wang, C. C. L., Martínez, J., McMains, S., Alexa, M., Wyvill, B., and Lefebvre, S. (2019). Curvislicer: slightly curved slicing for 3-axis printers. *ACM Trans. Graph.*, 38(4).

Ezair, B., Fuhrmann, S., and Elber, G. (2018). Volumetric covering print-paths for additive manufacturing of 3d models. *Computer-Aided Design*, 100:1 – 13.

Fang, G., Tianyu, Z., Zhong, S., Chen, X., Zhong, Z., and Wang, C. (2020). Reinforced fdm: multi-axis filament alignment with controlled anisotropic strength. *ACM Transactions on Graphics*, 39:1–15.

Fang, G., Zhang, T., Huang, Y., Zhang, Z., Masania, K., and Wang, C. C. (2024). Exceptional mechanical performance by spatial printing with continuous fiber: Curved slicing, toolpath generation and physical verification. *Additive Manufacturing*, 82:104048.

Fowler, R. M., Maselli, A., Pluimers, P., Magleby, S. P., and Howell, L. L. (2014). Flex-16: A large-displacement monolithic compliant rotational hinge. *Mechanism and Machine Theory*, 82:203–217.

G, L. S., Pawel, M., Marius, L., and Faller, L. M. (2023). Supportless 5-axis 3d-printing and conformal slicing: A simulation-based approach. In *2023 24th International Conference on Thermal, Mechanical and Multi-Physics Simulation and Experiments in Microelectronics and Microsystems (EuroSimE)*, pages 1–7.

Ge, L., Dong, L., Wang, D., Ge, Q., and Gu, G. (2018). A digital light processing 3D printer for fast and high-precision fabrication of soft pneumatic actuators. *Sensors and Actuators A: Physical*, 273:285–292.

Guennebaud, G., Jacob, B., et al. (2010). Eigen v3. http://eigen.tuxfamily.org.

Guidetti, X., Balta, E. C., Nagel, Y., Yin, H., Rupenyan, A., and Lygeros, J. (2023). Stress flow guided non-planar print trajectory optimization for additive manufacturing of anisotropic polymers. *Additive Manufacturing*, 72:103628.

Hirano, J., Tanaka, D., Watanabe, T., and Nakamura, T. (2014). Development of delta robot driven by pneumatic artificial muscles. In *2014 IEEE/ASME International Conference on Advanced Intelligent Mechatronics*, pages 1400–1405, Besançon, France.

Hong, F., Hodges, S., Myant, C., and Boyle, D. E. (2022). Open5x: Accessible 5-axis 3d printing and conformal slicing. In *Extended Abstracts of the 2022 CHI Conference on Human Factors in Computing Systems*, CHI EA '22, New York, NY, USA. Association for Computing Machinery.

Hornus, S. and Lefebvre, S. (2018). Iterative carving for self-supporting 3D printed cavities. In *Eurographics 2018 - Short Papers*, Delft, Netherlands.

Howell, L. L. (2001). *Compliant Mechanisms*. John Wiley and Sons, London, UK.

Howell, L. L., Magleby, S. P., and Olsen, B. M. (2013). *Handbook of Compliant Mechanisms*. Wiley. Cited by: 433.

Hsiao, H., Sun, J., Zhang, H., and Zhao, J. (2022). A mechanically intelligent and passive gripper for aerial perching and grasping. *IEEE/ASME Transactions on Mechatronics*, 27(6):5243–5253.

Huss, J. M. and Erdman, A. G. (2023). Gravity Augmented Fused Filament Fabrication Additive Manufacturing. *Journal of Medical Devices*, 17(2):021003.

Kargar, S. M. and Berselli, G. (2024). Tricom gripper–part i: Mechanical design and synthesis of a 3-finger compliant monolithic gripper. In *2024 20th IEEE/ASME International Conference on Mechatronic and Embedded Systems and Applications (MESA)*, pages 1–6.

Kargar, S. M., Parmiggiani, A., Baggetta, M., Ottonello, E., Hao, G., and Berselli, G. (2024). Optimization of a tetrahedron compliant spherical joint via computer-aided-engineering tools. *International Journal of Advanced Manufacturing Technology*, 132:1151–1162.

Kiener, L., Saudan, H., Cosandier, F., Perruchoud, G., and Spanoudakis, P. (2019). Innovative concept of compliant mechanisms made by additive manufacturing. *MATEC Web of Conferences*, 304:07002.

King, T. S. and Levey, K. R. (2010). Push/push latch.

Kipping, J. and Schüppstuhl, T. (2023). Load-oriented nonplanar additive manufacturing method for optimized continuous carbon fiber parts. *Materials*, 16(3).

Kodnongbua, M., Good, I., Lou, Y., Lipton, J., and Schulz, A. (2022). Computational design of passive grippers. *ACM Trans. Graph.*, 41(4).

Lau, T. Y., Chen, L., He, D., Li, Z., and Tang, K. (2023). Partition-based print sequence planning and adaptive slicing for scalar field-based multi-axis additive manufacturing. *Computer-Aided Design*, 163:103576.

Lettori, J., Raffaeli, R., Borsato, M., Peruzzini, M., and Pellicciari, M. (2024). Implementation and virtual assessment of a non-uniform cylindrical slicing algorithm for robot-based additive manufacturing. *The International Journal of Advanced Manufacturing Technology*, pages 1–22.

Liu, B., Feng, J., Lin, Z., Wu, S., He, Y., and Fu, J. (2024). Spherical path planning for multi axis support free additive manufacturing of truss structures. *Journal of Manufacturing Processes*, 109:198–212.

Lobontiu, N. (2001). *Compliant Mechanisms : Design of Flexure Hinges*. CRC Press, Boca Raton, Florida, USA.

Louis, M. S. (2003). Push-push latch.

Lussenburg, K., Sakes, A., and Breedveld, P. (2021a). Design of non-assembly mechanisms: A state-of-the-art review. *Additive Manufacturing*, 39:101846.

Lussenburg, K., Sakes, A., and Breedveld, P. (2021b). Design of non-assembly mechanisms: A state-of-the-art review. *Additive Manufacturing*, 39:101846.

Ma, R., Belter, J., and Dollar, A. (2015). Hybrid deposition manufacturing: Design strategies for multimaterial mechanisms via three-dimensional printing and material deposition. *Journal of Mechanisms and Robotics*, 7:021002.

Ma, R. and Dollar, A. (2017). Yale openhand project: Optimizing open-source hand designs for ease of fabrication and adoption. *IEEE Robotics & Automation Magazine*, 24(1):32–40.

Mannam, P., Kroemer, O., and Temel, F. (2021a). Characterization of compliant parallelogram links for 3d-printed delta manipulators. In *International Symposium on Experimental Robotics*, pages 75–84, Malta.

Mannam, P., Rudich, A., Zhang, K., Veloso, M. M., Kroemer, O., and Temel, F. Z. (2021b). A low-cost compliant gripper using cooperative mini-delta robots for dexterous manipulation. In *Robotics: Science and Systems XVII*, Held virtually.

Mcclintock, H., Fatma, Temel, Z., Doshi, N., Koh, J.-S., and Wood, R. J. (2018). The millidelta: A high-bandwidth, high-precision, millimeter-scale delta robot. *Science Robotics*, 3(14):eaar3018.

McGowan, P. and Hao, G. (2022). Design of a morphing compliant mechanism with separate gripping and retraction modes using a single actuation. *Journal of Mechanisms and Robotics*, 15.

Muscato, G., Prestifilippo, M., Abbate, N., and Rizzuto, I. (2005). A prototype of an orange picking robot: Past history, the new robot and experimental results. *Industrial Robot: An International Journal*, 32:128–138.

Naves, M., Nijenhuis, M., Seinhorst, B., Hakvoort, W., and Brouwer, D. (2021). T-flex: A fully flexure-based large range of motion precision hexapod. *Precision Engineering*, 72:912–928.

Nishimura, T. (1988). Push latch device.

Okunevich, I., Trinitatova, D., Kopanev, P., and Tsetserukou, D. (2021). Deltacharger: Charging robot with inverted delta mechanism and cnn-driven high fidelity tactile perception for precise 3d positioning. *IEEE Robotics and Automation Letters*, 6(4):7604–7610.

Palmer, M. and Laliberte, J. (2023). Effects of non-planar slicing techniques and carbon fibre material additives on the mechanical properties of 3d-printed drone propellers. *Drone Systems and Applications*, 11:1–11.

Patil, S., Alvares, S. C., Mannam, P., Kroemer, O., and Temel, F. Z. (2022). Deltaz: An accessible compliant delta robot manipulator for research and education. In *IEEE/RSJ Int. Conf. on Intelligent Robots and Systems (IROS)*, pages 13213–13219, Kyoto, Japan.

Pérez, P., Gangnet, M., and Blake, A. (2003). Poisson image editing. *ACM Trans. Graph.*, 22(3):313–318.

Petterson, A., Ohlsson, T., Caldwell, D., Davis, S., Gray, J., and Dodd, T. (2010). A bernoulli principle gripper for handling of planar and 3D (food) products. *Industrial Robot: An International Journal*, 37:518–526.

Pérez-Castillo, J. L., Mora, A., Perez-Santiago, R., Roman-Flores, A., Ahmad, R., and Cuan-Urquizo, E. (2023). Flexural properties of lattices fabricated with planar and curved layered fused filament fabrication. *Materials*, 16(9).

Raatz, A., Wrege, J., Soetebier, S., and Hesselbach, J. (2004). High precision compliant parallel robot with an optimized large workspace. In *International Design Engineering Technical Conferences and Computers and Information in Engineering Conference (IDETC-CIE)*, pages 1007–1014, Salt Lake City, Utah, USA.

Rommers, J., van der Wijk, V., and Herder, J. L. (2021). A new type of spherical flexure joint based on tetrahedron elements. *Precision Engineering*, 71:130–140.

Seino, A., Tokuda, F., Kobayashi, A., and Kosuge, K. (2024). Passive actuator-less gripper for pick-and-place of a piece of fabric.

Shan, Y., Shui, Y., Hua, J., and Mao, H. (2023). Additive manufacturing of non-planar layers using isothermal surface slicing. *Journal of Manufacturing Processes*, 86:326–335.

Song, H.-C., Ray, N., Sokolov, D., and Lefebvre, S. (2016). Anti-aliasing for fused filament deposition. *Computer-Aided Design*, 89:25 – 34. 14 pages, 22 figures.

Sreetharan, P. S., Whitney, J. P., Strauss, M. D., and Wood, R. J. (2012). Monolithic fabrication of millimeter-scale machines. *Journal of Micromechanics and Microengineering*, 22(5):055027.

Staicu, S. (2019). *Dynamics of Parallel Robots*. Springer International Publishing, Cham, Switzerland.

Su, X., Yang, Y., Xiao, D., and Chen, y. (2012). Processability investigatation of non-assembly mechanisms for powder bed fusion process. *The International Journal of Advanced Manufacturing Technology*, 64.

Tang, P., Zhao, X., Shi, H., Hu, B., Ding, J., Yang, B., and Xu, W. (2024). A review of multi-axis additive manufacturing: Potential, opportunity and challenge. *Additive Manufacturing*, 83:104075.

Tsugami, Y. and Nishida, T. (2017). Simple structured gripper using electromagnet and permanent magnet. In *Simple Structured Gripper Using Electromagnet and Permanent Magnet*.

Vanaei, H. R., Magri, A. E., Rastak, M. A., Vanaei, S., Vaudreuil, S., and Tcharkhtchi, A. (2022). Numerical - experimental analysis toward the strain rate sensitivity of 3D-printed nylon reinforced by short carbon fiber. *Materials*, 15(24).

Venkiteswaran, V. K. and Su, H.-J. (2015). A parameter optimization framework for determining the pseudo-rigid-body model of cantilever-beams. *Precision Engineering*, 40:46–54.

Wang, R., Zhang, X., Zhu, B., Hongchuan, Z., Chen, B., and Wang, H. (2020). Topology optimization of a cable-driven soft robotic gripper. *Structural and Multidisciplinary Optimization*, 62.

Xiao, B., Alamdar, A., Song, K., Ebrahimi, A., Gehlbach, P., Taylor, R. H., and Iordachita, I. (2022). Delta robot kinematic calibration for precise robot-assisted retinal surgery. In *2022 International Symposium on Medical Robotics, ISMR 2022*, pages 1–7, Atlanta, GA, USA. Institute of Electrical and Electronics Engineers Inc.

Zhang, M., Zhang, J., Yang, D., Li, Y., Cui, X., and Fu, K. (2024). Improved interlayer performance of short carbon fiber reinforced composites with bio-inspired structured interfaces. *Additive Manufacturing*, 79:103936.

Zhang, T., Fang, G., Huang, Y., Dutta, N., Lefebvre, S., Kilic, Z. M., and Wang, C. C. L. (2022). S3-slicer: A general slicing framework for multi-axis 3d printing. *ACM Trans. Graph.*, 41(6).

Zhao, D., Han, Y., Zhu, G., and Guo, W. (2023). Dimension synthesis of a 2t2r curved layer fdm 3d printer. *Proceedings of the Institution of Mechanical Engineers, Part C: Journal of Mechanical Engineering Science*, 0(0):09544062231165211.

Appendix A

DuraFormPA cyclic material characterisation

In light of the observations from stiffness tests, which indicated the presence of hysteretic behaviour, a focused testing campaign was conducted to evaluate this phenomenon in greater detail. The hysteresis testing was executed by subjecting dogbone specimens to a repetitive stretching up to 4[mm] of deformation and subsequent releasing process.

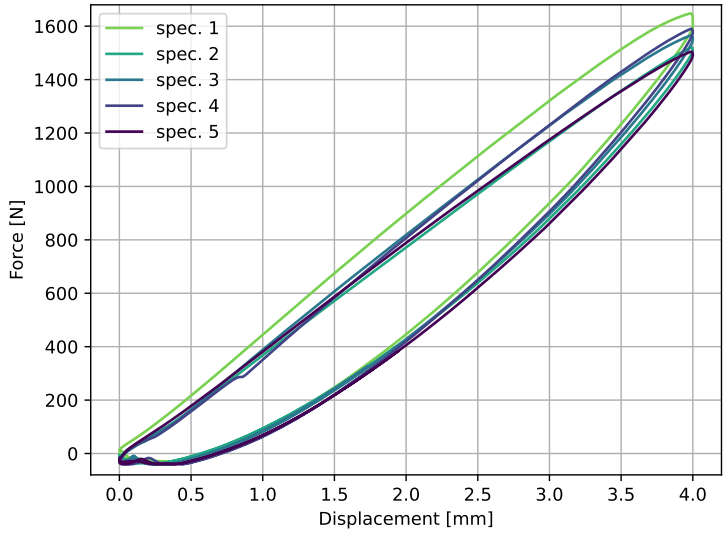

Figure A.1 Results of the hysteresis test. The figure shows the tensile loading and unloading curves one of the five specimens (a), as described in the main text. The acquired data are colour coded on the basis of their acquisition time; clearer colours correspond to the first cycles and darker colours correspond to the last.

A total of five specimens were subjected to this procedure, each undergoing five complete cycles. The specimens adhered to the specific geometric requirements stipulated in the ISO 572 standard, with a cross-section of 4[mm] by 9[mm]. All of these tests were conducted using the same Zwick-Roell Z050 machine, which had previously been utilised for the evaluation of the DeltaFlex's stiffness.

The results of this test are shown in Fig.A.1. The results clearly demonstrate that all examined samples exhibited prominent hysteretic behaviour. For all specimens the width of the hysteresis cycles eventually stabilises after the third and fourth cycle. Furthermore, the loading and unloading curves do not follow straight paths thus suggesting a discernible degree of non-linearity in the material's response.

Appendix B

Configurations photos

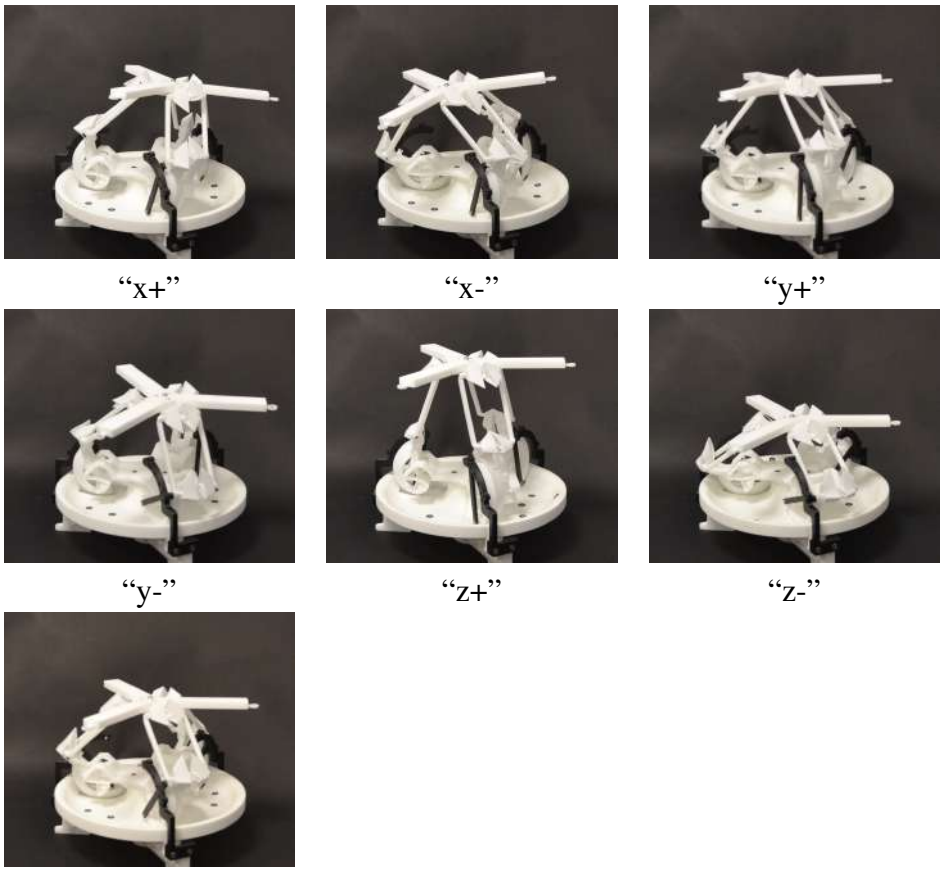

Figure B.1 Reference test configurations. The figure shows seven photographs of the mechanism fixed into the six reference test configurations, and the “home configuration.